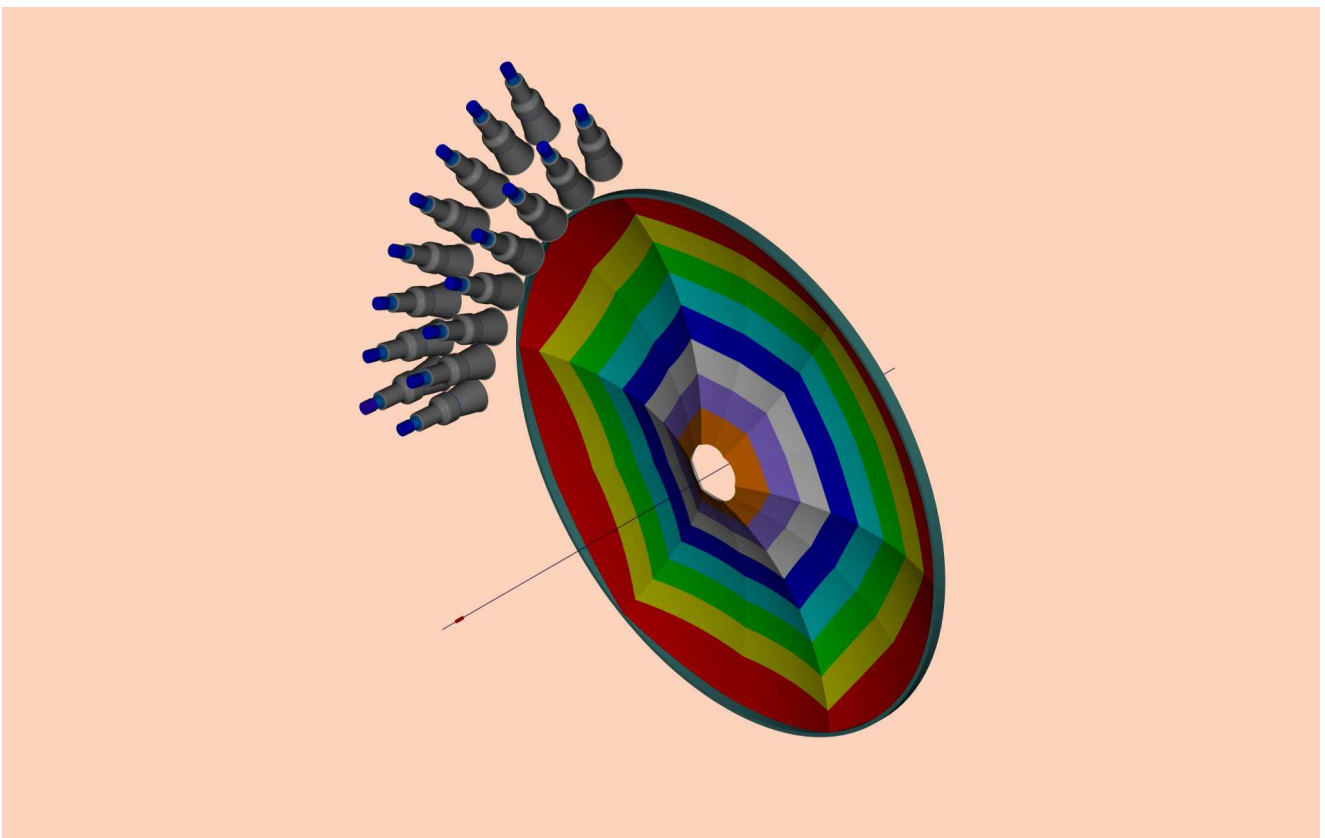


The CLAS12 High Threshold Cerenkov Detector Technical Design Report



Version 1.1

The CLAS12 High Threshold Cerenkov Detector

Technical Design Report

I.Bedlinskiy¹, S.Boyarinov², V.Burkert², S.Christo³, L.Elouadrhiri², G.Fedotov⁴,
K.Hafidi⁵, P.Hemler², G.Jacobs², J.Joo⁶, D.Kashy², V. Kubarovskiy⁷,
K.Mikhaylov¹ J.Price⁸, Y. Sharabian*², P.Stoler⁷, A. Vlassov¹,
C. Wiggins², M.Zarecky²

May 11, 2007

¹Institute of Theoretical and Experimental Physics, Moscow, 117259, Russia

²Thomas Jefferson National Accelerator Facility, Newport News, Virginia 23606

³Christopher Newport University, Newport News, Virginia 23606

⁴Moscow State University, General Nuclear Physics Institute, 119899 Moscow, Russia

⁵Argonne National Laboratory, Argonne, Illinois, 60430

⁶University of Connecticut, Storrs, Connecticut 06269

⁷Rensselaer Polytechnic Institute, Troy, New York 12180-3590

⁸University of California at Los Angeles, Los Angeles, California 90095-1547

Contents

1	Introduction	3
1.1	Optical Requirements	4
1.2	Physical Environment	6
1.3	Overall design	8
2	Optical Design and Construction	9
2.1	Mirror Prototyping	14
2.2	Light Collection Cones.	24
3	DAQ for HTCC	28
4	HTCC Gas System Overview	30
5	Simulations of Detector Peformance	32
5.1	Optical Properties of physical components	32
5.1.1	Radiator Gas	33
5.1.2	Photomultiplier Tubes (PMT)	33
5.2	Distributions of Photons incident on the PMT faces.	33
5.3	Background Rates	35
6	PMT Studies	36
6.1	PMT magnetic shielding studies	36
6.2	PMT Laboratory Studies.	38
6.2.1	Cosmic Ray PMT Testing Apparatus.	44
6.3	Calibration of the ADC scale	47
6.4	Relative Quantum Efficiency Measurements	52
7	Mechanical Design	54
7.1	Outer body	54
7.2	PMT Mount	55
7.3	Mirror positioning and alignment	56
7.4	Upstream and entry	56
7.5	Exit Scheme.	57

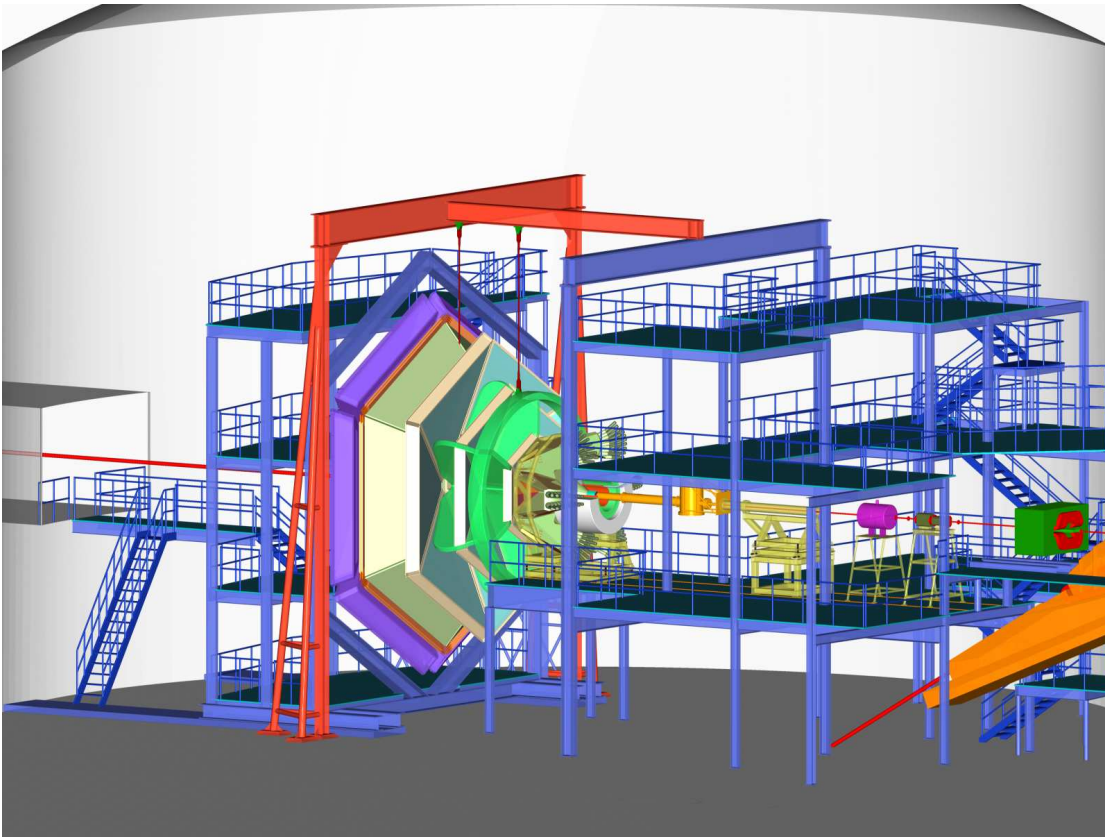


Figure 1: CLAS12 spectrometer in the experimental Hall B. In light green is shown Torus Magnet, Central Detector and HTCC are mounted on the extension of Level I of the Main Frame

1 Introduction

The High Threshold Čerenkov Counter (HTCC) is one of the major components of the CLAS12 spectrometer. It will be used for electron identification in all experiments with electron beams. In combination with the Low Threshold Čerenkov Counter (LTCC) it will make possible the identification of charged π -mesons over the entire momentum range up to a maximum of 5 GeV^2/c^2 . An overall view of the CLAS12 spectrometer is given in Figure 1. Part of the infrastructure in the Hall B experimental area and other equipment are shown as well.

The HTCC is located between the Central and Forward Detectors of CLAS12, and mounted on a separate cart that can be moved along beam direction.

The radiating gas for the HTCC is CO_2 gas at room temperature and pressure. The threshold of the detection of charged π -mesons is $4.9\text{GeV}/\text{c}$, and in the entire momentum

range below the threshold the rejection factor for pions is greater than 2000. The optical configuration in the HTCC is chosen to be similar to LTCC currently used in CLAS. However, since the detector is positioned upstream of the drift chambers, it was decided to use one reflection from mirror per module, as opposed to two for the LTCC. The current design comprises 96 light reflection and collection modules.

The main working parameters of the HTCC are given below:

Channels	96 (6 sectors of (2×8) channels each)
Working Gas	CO₂ @ 1atm and room temperature
Mirror Type	Ellipsoidal, 96 segments
Photomultipliers	XP4508 (5", Quartz face plate)
Threshold	4.9GeV/c (π-mesons)
Threshold	15GeV/c (electrons)
Rejection Factor	> 2000 at $p < 4.9\text{GeV}/c$

The overall performance requirements and scope of primary problems which need to be solved are shown in the following table:

Performance Requirement	Regarding R&D tasks to be addressed
High electron detection efficiency	Development of a technology providing highest finish of mirror surfaces at low cost
Run at luminosity $\geq 10^{35} \text{ cm}^2 \times \text{sec}$	Flexibility in distributing angular acceptance over adjacent channels
Acceptance $\Delta\phi = 2\pi$ in angular range $5^\circ \leq \theta \leq 35^\circ$	Designing mirrors with no support/alignment parts within acceptance. No dead zones between mirror segments
Total Thickness $\leq 200\text{mg/cm}^2$	Developing technology of mirror construction using materials of low density and no residual stress
Reliability	Maintenance free mirror. PMTs, other components can be reached and replaced if necessary in situ

1.1 Optical Requirements

The upgraded CLAS12 spectrometer incorporates several major components inherited from CLAS such as the Forward Time-of-Flight Counters, the Low Threshold Čerenkov Counter,

and Forward Electromagnetic Calorimeter. CLAS12 will be built in the same experimental area. This places constraints on the overall CLAS12 design and consequently on all detector components while requiring most efficient acceptance coverage.

The HTCC occupies very limited space downstream of the Central Detector and is mounted between the Microstrip Silicon Tracker and Region I drift chambers. Figure 2 illustrates the basic optics of the detector, and Figure 3 shows a 3-dimensional view of the mirror and PMTs for one sector. The design is such that the photons are reflected only once by one of the elliptical mirrors and then directly impinge on the photocathode of photomultiplier tube. However, since the optical design must be forgiving in the sense that the light collection efficiency must be relatively insensitive to target length and position, smearing of photon distribution due to the influence of the magnetic fields of the Central Solenoid on the particle trajectories, the 5 inch photomultiplier tubes are equipped with *Winston* light collection cones.

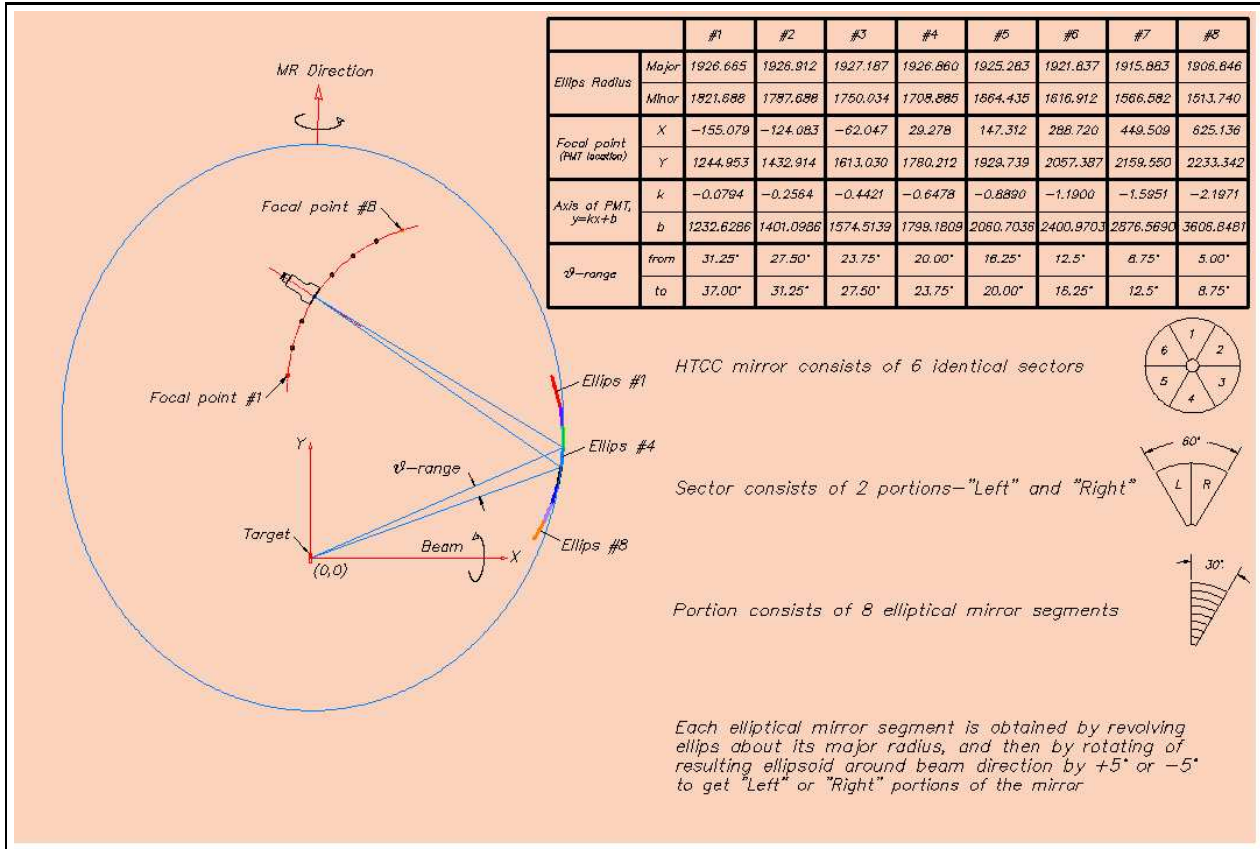


Figure 2: Geometry and main parameters of HTCC

The optical properties of the mirrors, Winston cones and photomultiplier tubes are optimized for maximum reflection and detection of the Čerenkov light. Since much of the Čerenkov light is in the ultra violet (UV), the working surfaces of mirrors and cones will consist of evap-

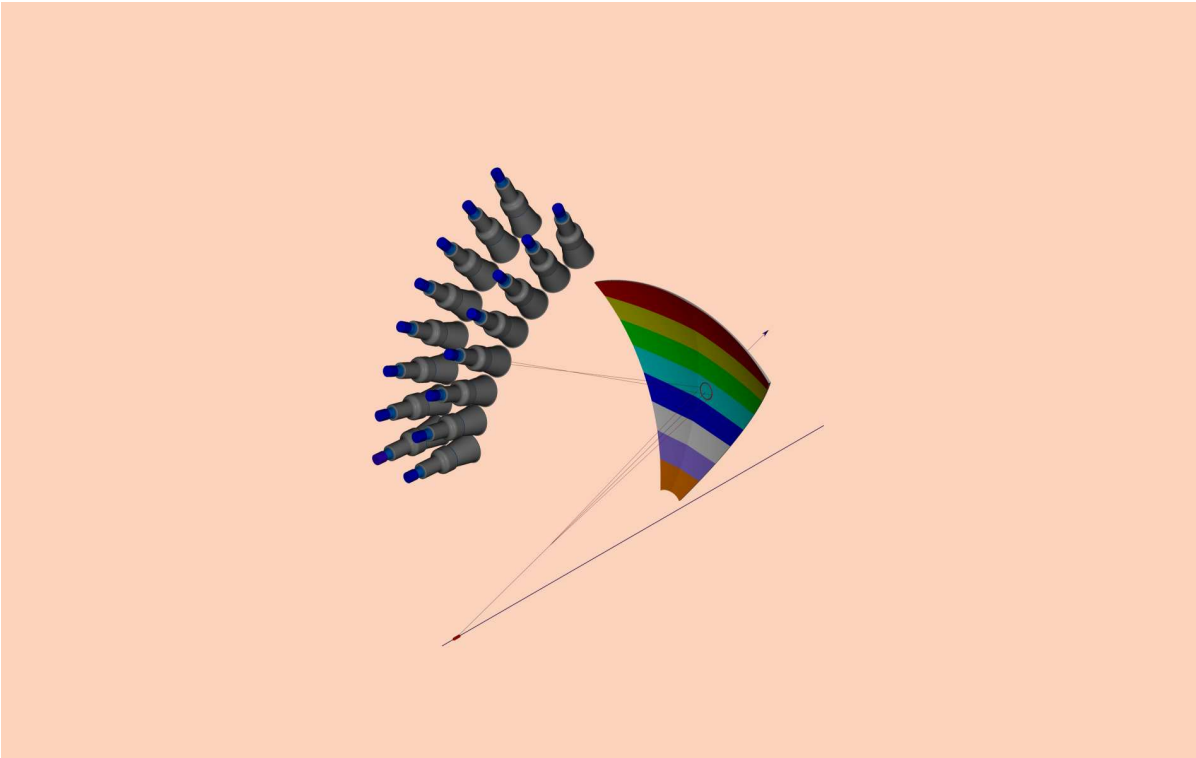


Figure 3: 3D-view of mirror and PMTs for one sector

orated coatings of aluminum, which has a high reflectivity from the near UV through the visible wavelength regions. An evaporated magnesium fluoride (MgF_2) protective coating will be provided to prevent oxidation of the aluminum, while transmitting light through the required wavelength range. The photomultiplier tubes (PMT) will be the Photonis XP4508 with quartz face plates, again, to maximize efficiency in the UV range.

1.2 Physical Environment

The HTCC is a single module detector covering all six sectors for scattering angles in the range $\theta = 5^\circ$ to 35° in the entire $\Delta\varphi = 2\pi$ range. Since the Detector is a single unit it can be moved along the beam direction or removed from the beam if necessary. It is located in a strong magnetic field of the superconducting solenoid of the Central Detector. The light collection geometry of the HTCC is such that all 96 photomultiplier tubes are located in the fringe field domain at radial distances of 124.5cm or greater from the electron beam. These distances are chosen to be maximal while still small enough to fit in the Hall B main frame infrastructure (Figure 4) and to allow moving the detector upstream for CLAS12 alignment and maintenance purposes.

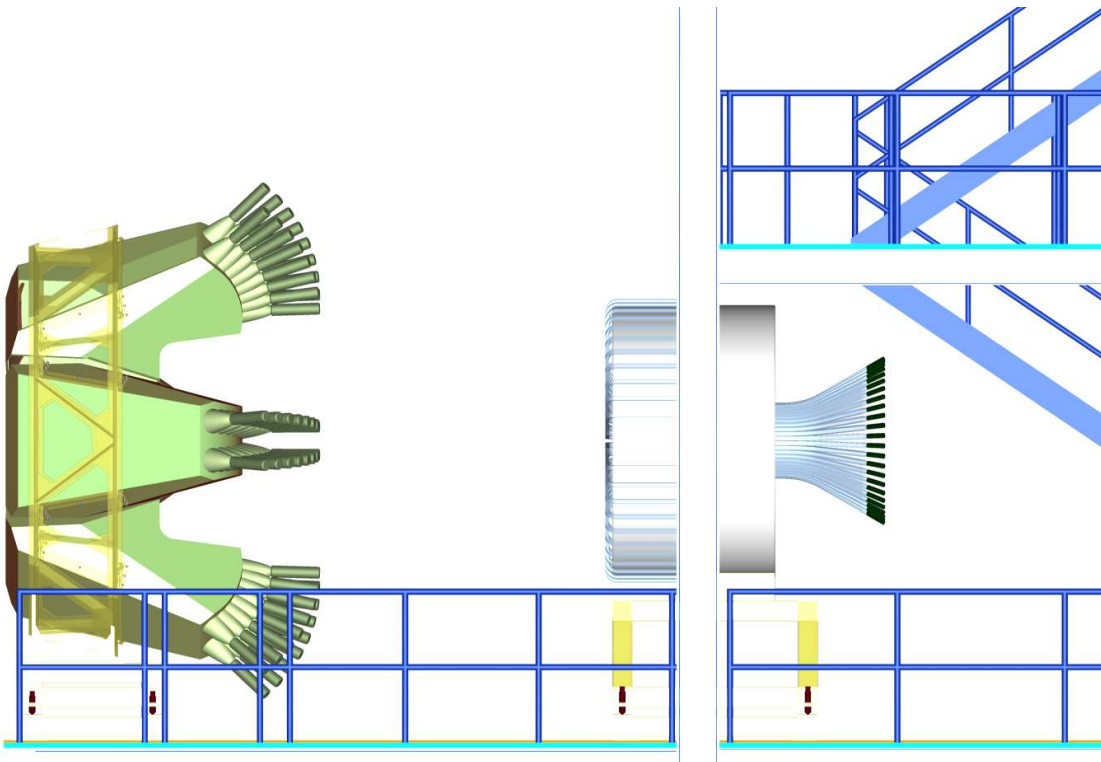


Figure 4: HTCC and Central Detector (moved upstream under Main Frame)

The space of the HTCC along the beam direction defines the intensity of the Čerenkov photons expected at a given pressure of working gas. The design of CLAS12 specifies that the entry window of Čerenkov Counter is located at $\sim 0.5''$ distance downstream of the SVT of the Central Detector, and the exit window is 10cm upstream of the Region 1 drift chambers. That leaves distances that scattered electrons travel in the CO₂ radiator ~ 131 cm at $\theta = 5^\circ$ and ~ 181 cm at $\theta = 35^\circ$. The geometry of the HTCC is optimized to keep difference in path lengths minimal. The distribution of magnetic fringe field were taken into consideration in locating the PMTs. The detailed optical geometry and estimated signal strength is discussed in detail later in Section 3.2.

The intrinsic angular and momentum resolutions of CLAS12 along with its capability of running at high luminosities puts serious constraints on both the thicknesses and materials that can be used in HTCC mirrors. These limitations on materials and estimates of required and achievable thicknesses are given in Section 2.1.

Another constraint comes from the acceptance specifications for Regions 1, 2 and 3 (R1,R2 and R3 respectively) drift chambers which are located downstream of the HTCC. The polar angle acceptance for the drift chambers $\theta = 5^\circ$ to 40° is greater than for the HTCC. The support structure for the elliptical mirrors has to be located in the relatively narrow *shadow*

region of the coil planes of CLAS12 Torus Magnet, and the mirror substrate support built of as light materials as possible.

1.3 Overall design

The overall approach to working out HTCC design is a twofold task, first to outline general demands on the HTCC performance and then define ranges for critical parameters of the major components such elliptical mirrors.

The main requirements are:

- High electron detection efficiency, low background
- Capability of running at luminosity $\mathcal{L} \geq 10^{35} \text{ cm}^{-2} \times \text{sec}^{-1}$
- Angular acceptance $5^\circ \leq \theta \leq 35^\circ$ and $\Delta\varphi \approx 2\pi$
- Lightweight, as little material as possible within acceptance to meet the expected angular and momentum resolutions of CLAS12, $-\delta\theta \leq 1.5 \text{ mrad}$, $\delta\varphi \leq 5 \text{ mrad}$, and $\Delta p/p \leq 1\%$

The view of HTCC is given in Figure 5.

A detailed description of the current status of the detector design is provided in Chapter 6. Some specific features are:

- Thin entry and exit windows of Black Kapton film ($\sim 3.5 \text{ mg/cm}^2$ and $\sim 11 \text{ mg/cm}^2$ respectively)
- Ultra thin self supporting mirror
- Capability of working with different types of high density Möller shields

Total radiation length of the detector is $\sim 1.6\%$ including contributions of CO₂ radiator, $\sim 0.8\%$, and of the mirror, which does not exceed 0.8%. Since the number of photons per event is proportional to a total radiation length of the radiator, the only way to decrease *thickness* of the detector without compromising its performance is to use thinner mirrors backing. Figures 6a,b and c illustrate the changes in CLAS12 resolution for different mirror thicknesses: standard ($\sim 200 \text{ mg/cm}^2$) and reduced to $\sim 100 \text{ mg/cm}^2$.

The results show a relatively small improvements in momentum, angular and spatial resolutions for thinner mirrors, indicating that the influence of mirror thickness is small or comparable with contributions of other CLAS12 detector components.

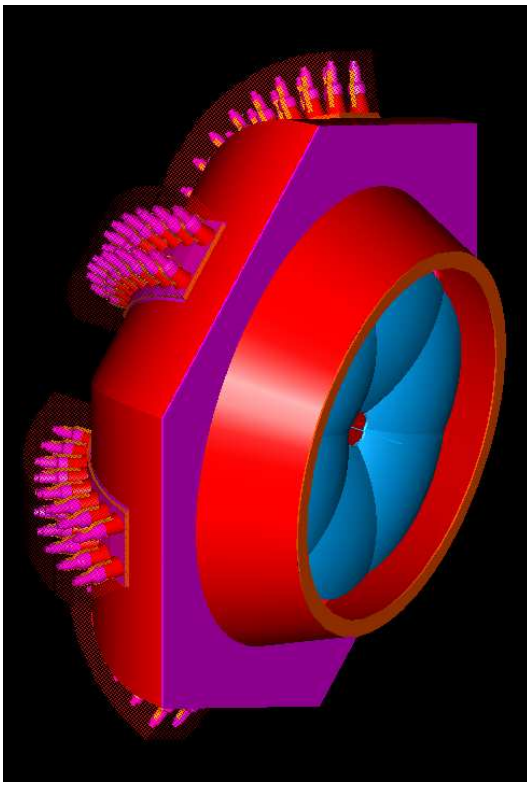


Figure 5: Back view of the HTCC, in blue shown Elliptical mirror

2 Optical Design and Construction

The most challenging aspect of the HTCC is the construction of the elliptical mirror. In addition to being very lightweight and self-supportive, there must not be shadowing among adjacent mirrors or gaps left between them. This problem has been worked out as follows:

Each mirror surface is an ellipsoid of rotation so the line of intersection of adjacent mirror surfaces is curved. If two coplanar ellipses intersect, revolving each ellipse about own major axis give two ellipsoids of rotation, (1) and (2), represented by following equations:

$$\frac{x^2 + (y - y_1)^2}{a_1^2} + \frac{(z - z_1)^2}{b_1^2} = 1 \quad (1)$$

$$\frac{x^2 + (y \cdot \cos\theta - z \cdot \sin\theta)^2}{a_2^2} + \frac{(y \cdot \sin\theta - z \cdot \cos\theta)^2}{b_2^2} = 1$$

where $(0, y_1, z_1)$ are coordinates of center of ellipse (1), a_1, a_2 and b_1, b_2 respectively are minor and major radiiuses of ellipses, θ is angle between major axis b_2 and OZ axis in YOZ-plane.

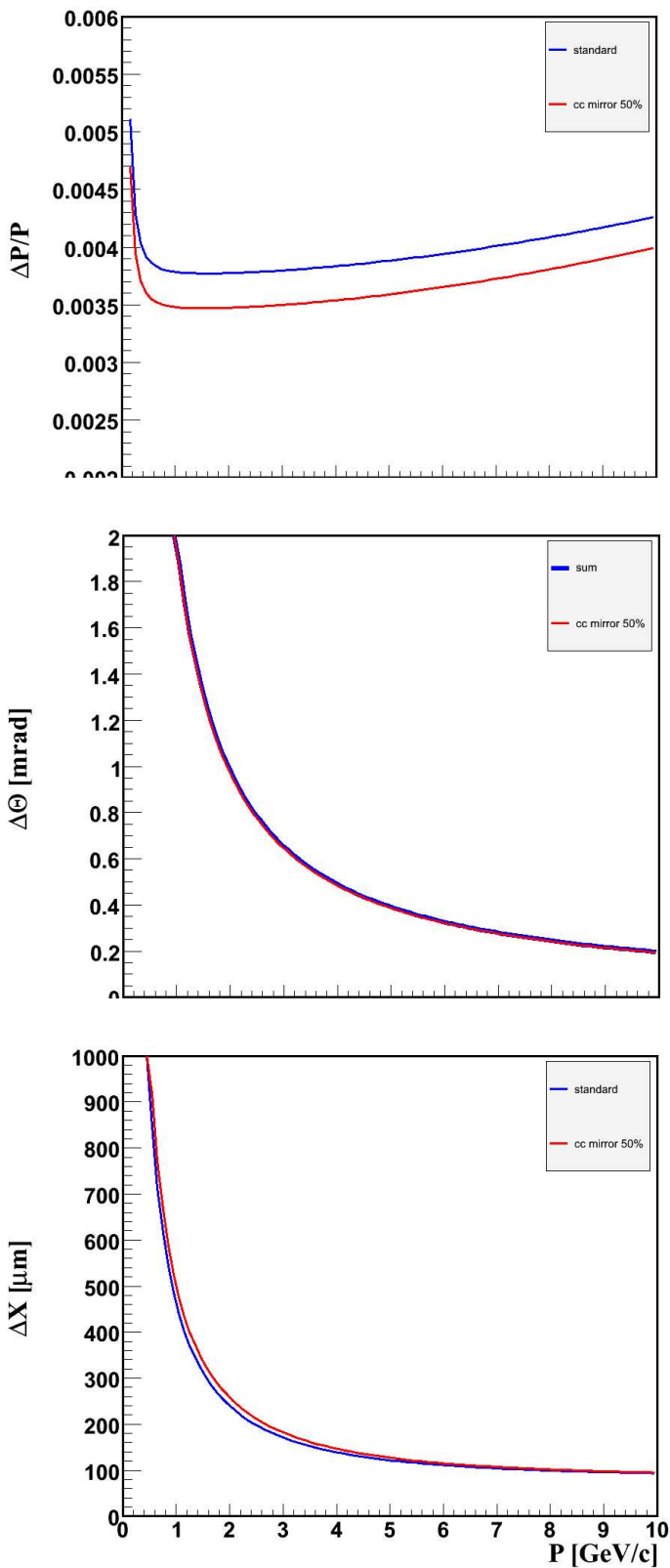


Figure 6: a -momentum, b- angular, and c -spatial resolution of CLAS12

Considering the system in $X = c < a_1$ plane, we get (assuming $a_1 < a_2$):

$$\begin{aligned} \frac{(y - y_1)^2}{a_1^2} + \frac{(z - z_1)^2}{b_1^2} &= c_1^2 \\ \frac{(y \cdot \cos\theta - z \cdot \sin\theta)^2}{a_2^2} + \frac{(y \cdot \sin\theta - z \cdot \cos\theta)^2}{b_2^2} &= c_2^2 \end{aligned} \quad (2)$$

By excluding one variable from (2) we arrive at a general quartic equation :

$$p_0 z^4 + p_1 z^3 + p_2 z^2 + p_3 z + p_4 = 0 \quad (3)$$

which always can be solved, and in the case of the HTCC geometry has two roots (see Figure 7). So, from (2) we obtain two points $P_1^{(c)}(y_1, z_1)$ and $P_2^{(c)}(y_2, z_2)$ in the plane $X = c$, which satisfy equation (1) as well at $x = c$: $P_1^{(c)}(c, y_1, z_1)$ and $P_2^{(c)}(c, y_2, z_2)$ are the roots of (1). Another two roots of (1) can be found at $x = 0$ (the YOZ-plane): $P_3(0, y_1, z_1)$ and $P_4(0, y_2, z_2)$. Three out of any four roots define a plane. It can be shown that the remaining root belongs to the same plane as well. Since we arbitrarily used $X = c$, all points of intersection (intersection curve) of the two ellipsoids belong to the same plane. This allows us to build mutually self-supporting elliptical mirrors in which there are no gaps or shadowing of one mirror by the next. As a result, the cutting of segments along the perimeter and final assembly become relatively simple. Moreover, there will be no shadowing of one mirror by another, no "dead" zones for any electrons from target within the acceptance. This also eliminates need of having a support structure for any single mirror segment and consequently makes it possible to construct the most efficient and lightweight mirror.

Figure 8 shows 8 intersecting mirrors forming half of the mirror array for one sector. In the table are given exact coordinates of points defining planes of intersection between segments and used in corresponding MC simulations. Figure 9 illustrates a concept of assembly. Approximate dimensions in inches of the mirror segments are given in the table.

Tolerances of construction are critical for the HTCC performance. Typical tolerances for cutting substrates are of the order of $0.001"$ and have been achieved in prototyping. So, the expected average deviation from the nominal geometry would be mostly due to the accuracy that can be achievable at the assembly stage. It is anticipated to keep the assembly tolerance within $\pm 0.010"$ for one mirror segment. Parallel shifts will not affect the light collection because of the large overall acceptance, whereas unwanted rotation of a segment during assembly might require some adjustment of PMT positions which would be unacceptable. At the given average width of segment, $\sim 5.60"$ (see Figure 9), the angular equivalent of $\pm 0.01"$

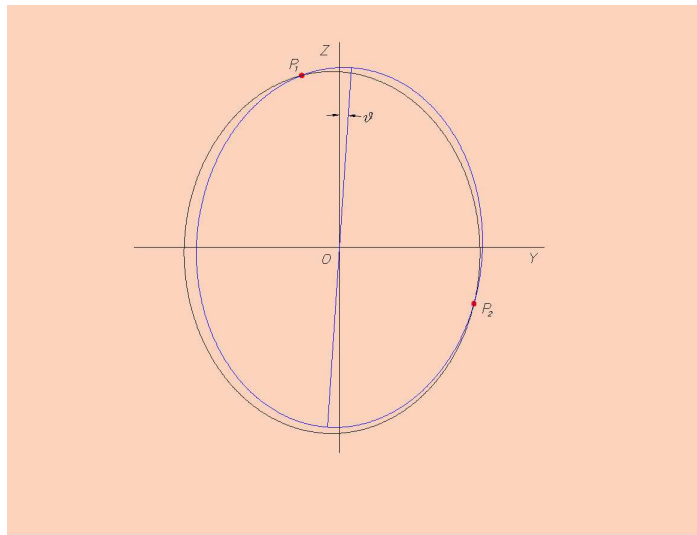


Figure 7: Ellipses of adjacent mirrors intersecting in two points

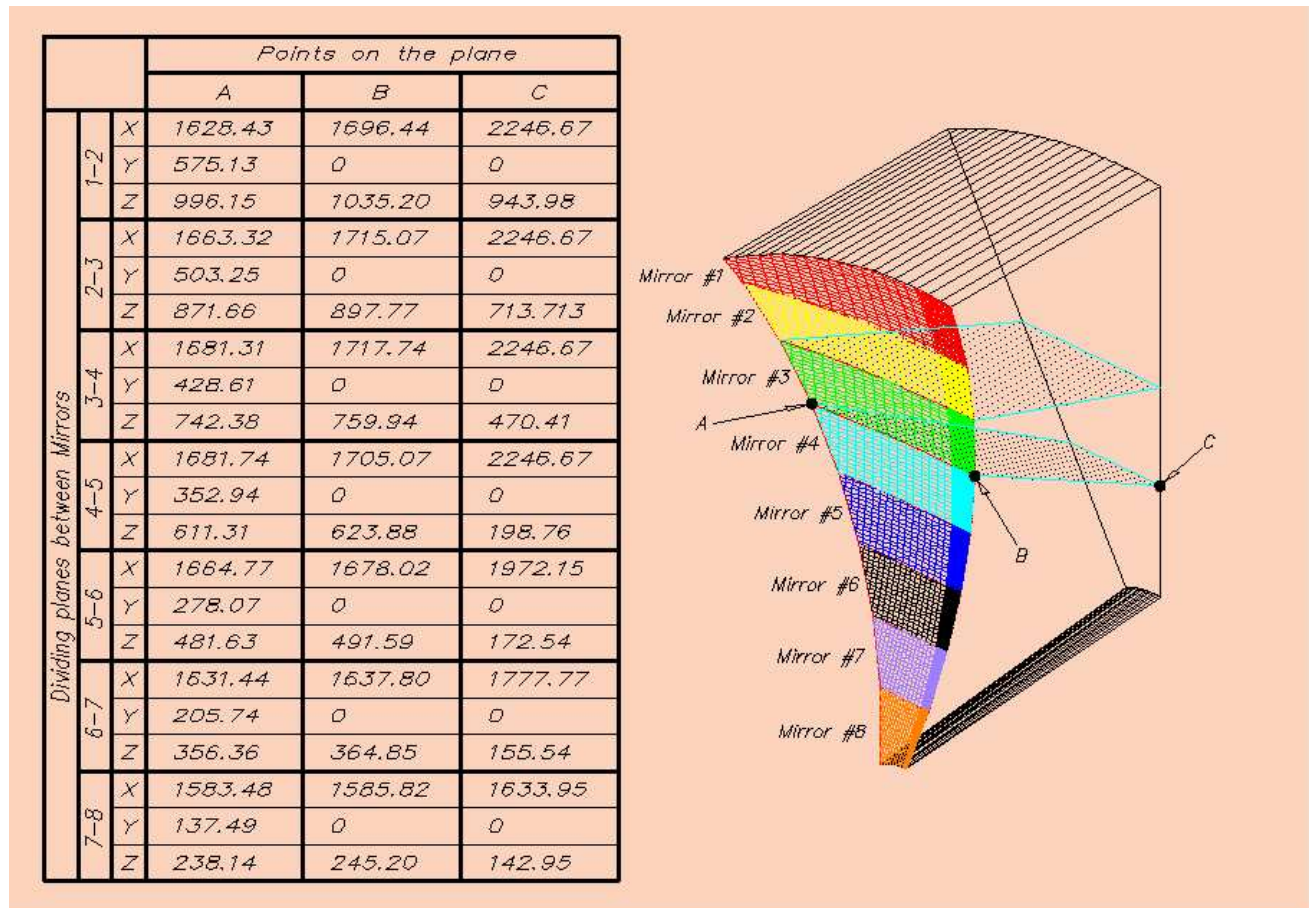


Figure 8: Planes of intersection of adjacent mirror segments

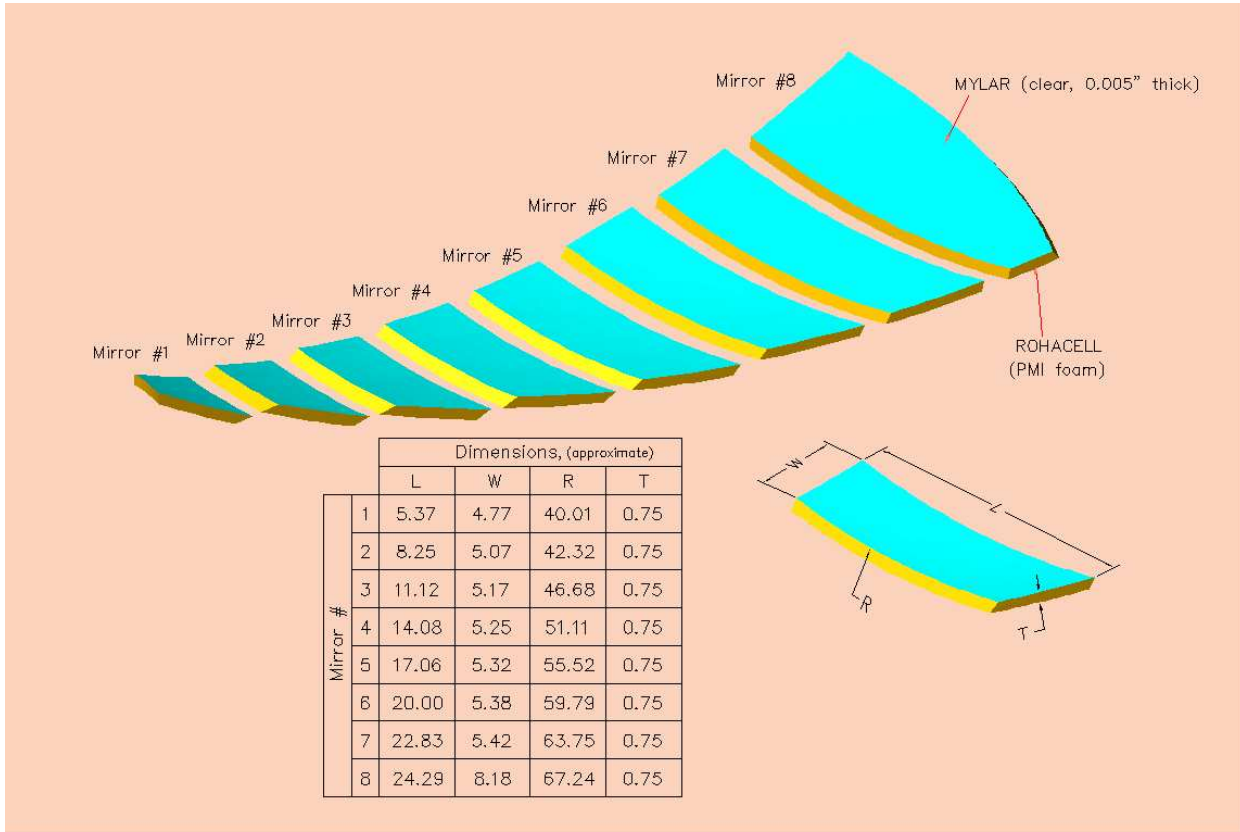


Figure 9: Elliptical mirror segments cut along planes of intersection. Set of 8 segments cover 1/2 of the acceptance of one sector. A mirror image of this set covers the other half of the acceptance.

is ~ 2 mrad or less. This is the worst possible case since all segments except of #1 are of length greater than 5.60". The average distance between mirrors and corresponding PMTs is $\sim 80.5"$. Therefore the shift of the image in the focal plane of PMT is less than 0.15" ($\sim 3.8\text{mm}$). This estimate is to be examined in R&D in 2007.

2.1 Mirror Prototyping

All main features of HTCC and properties of components are planned to be examined and checked by prototyping of key elements and testing. In this section we present results on prototyping of a mirror segment obtained in FY06, and describe current R&D efforts on building a mirror consisting of 3 mirror segments.

The main R&D goal is to find ways of building an elliptical mirror of

- 200mg/cm² of total thickness
- minimal residual stress (no adjustment in situ)
- highest possible finish of working surface
- reasonable cost

A mirror substrate consists of a thermally shaped plain Mylar film of thickness 0.0050", laminated to an ellipsoidal substrate made of rigid polymethacrylimide polymer foam Rohacell HF31 ($\rho \approx 31\text{mg/cm}^3$). In the entire construction procedure the working surface of the Mylar film stays untouched throughout all stages. The aluminum reflector and optical coating of magnesium fluoride (MgF_2) will be vacuum deposited onto the mylar surface after the the substrate and mylar are joined as a completed unit. A set of molding tools is used for shaping of Mylar film into the ellipsoidal shape which mates with the Rohacell substrate without residual stresses. One of the mold fixtures attached to the bottom plate is shown in Figure 10 . The top surface of the mold is cut to the exact shape of specified ellipsoid of rotation by computer controlled milling using a ball end mill. The thickness of film is taken into account. The top of the mold is then polished to remove scallops left after milling. The Mylar film is shaped by this surface, so the finish has to be smooth enough to avoid a *telegraph wire* effect, although the surface does not have to be of mirror quality.

For better control of the Mylar film edges and to minimize effects of thermal contraction a thin aluminum support guard is installed surrounding the mold, as shown in Figure 10. There is a small gap of 1/8" width left between the support and mold. The support has a profile

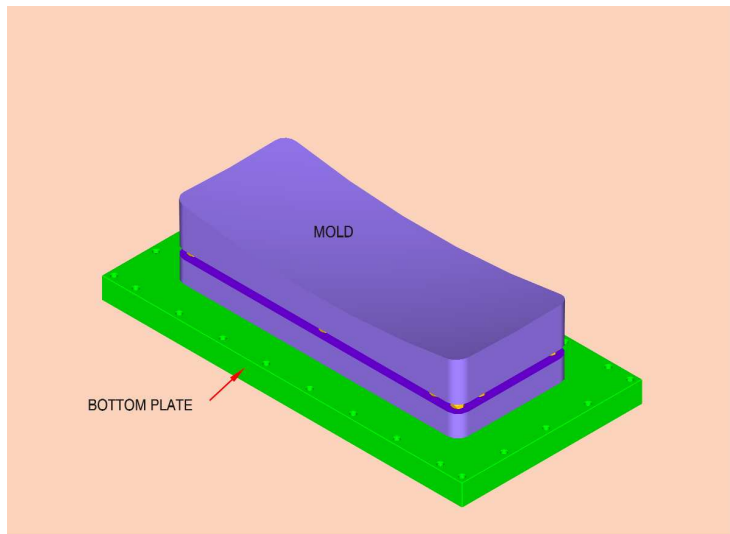


Figure 10: Mold installed on bottom plate

(shown in red) parallel to the edge of ellipsoidal surface of the mold. The gap is so small that the edge of shaped Mylar film is defined not by mold but by support. This results in a better alignment of the film with the foam substrate while gluing.

In Figure 12 the wall of the vacuum chamber attached to the bottom plate is shown. The wall has high temperature rated vacuum o-rings installed both on top and bottom.

The profile of the top of the wall is cylindrical, such that there is approximately constant clearance of $\sim 1/4"$ between this surface and ellipsoidal surface of the mold. The inside gap between the wall and support is quite wide. It has to be wide enough for the Mylar film to concave channels under applied pressure. These channels are formed all the way around the support and are necessary for tension relief when the chamber is being cooled down and then depressurized.

A portion of Mylar film is put on top of the vacuum chamber, as shown (in transparent yellow) on Figure 13. The top surface of the Mylar remains untouched during cutting and installation of the film. A flange is placed on the top of the Mylar and tightened down to the wall. Then the air in the chamber is pumped out so that the Mylar is deflected under atmospheric pressure, as in Figure 14.

At this point, while still at room temperature, the Mylar is touching the mold, and the area of contact between them is about 60-70% of maximum. To provide a 100% contact the vacuum chamber is heated in the oven to a temperature of 170°C. During the heating process, which takes about 4 hours, the chamber remains connected to a vacuum pump running outside the oven. To increase the deflection of the unsupported portion of Mylar film (along the wall)

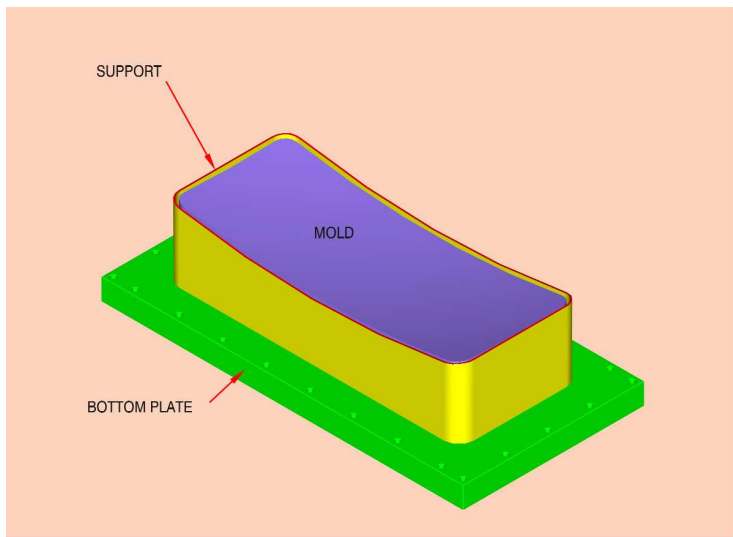


Figure 11: Support installed around mold

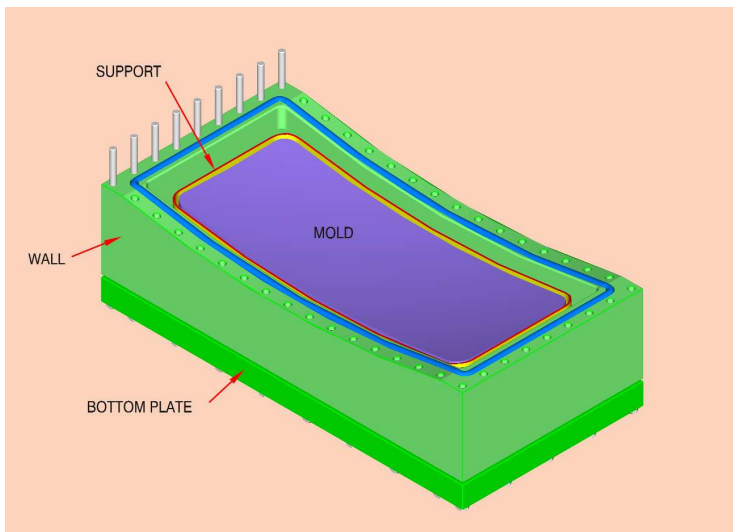


Figure 12: Vacuum chamber with mold

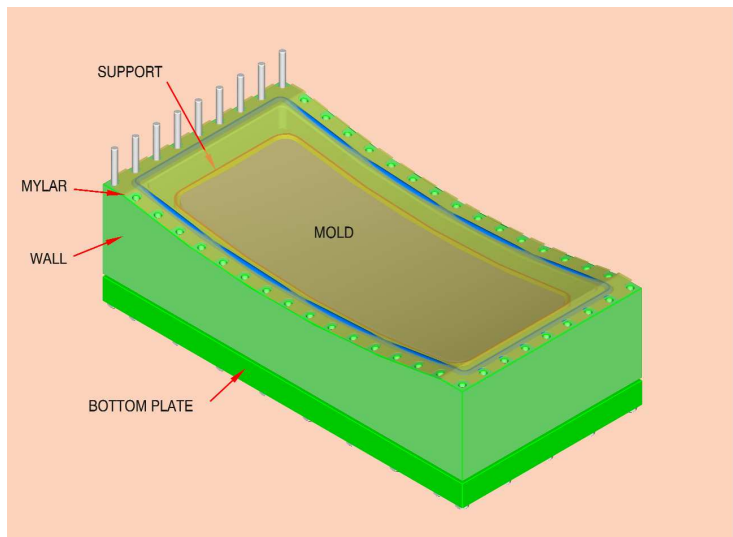


Figure 13: Vacuum chamber with mold and precut Mylar film

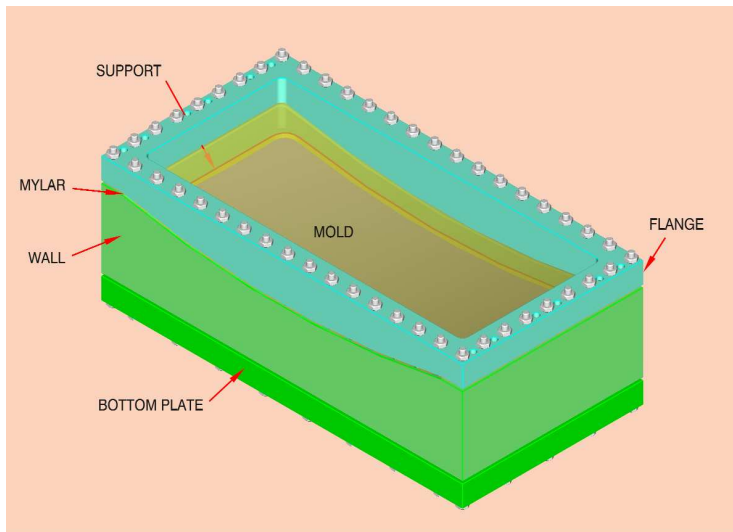


Figure 14: Vacuum chamber with mold and Mylar film

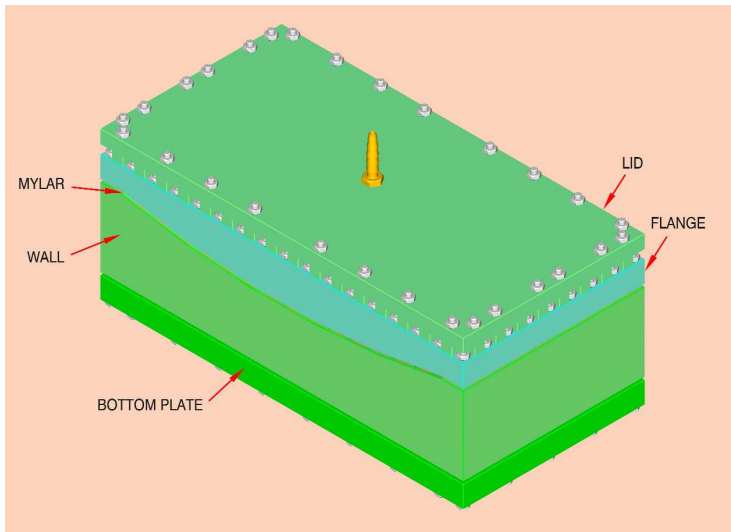


Figure 15: Vacuum chamber equipped with lid allowing molding of Mylar at higher pressures

additional pressure is applied to the film. This is done by covering the vacuum chamber with a lid installed on the top of flange, as shown in Figure 15. The volume under the lid is then pressurized with dry nitrogen.

The maximal differential pressure applied to the Mylar can be as high as 3 Kg/cm^2 . Tested stable results were obtained at differential pressures in the range 2.0 to 2.55 Kg/cm^2 , depending on temperature. The cooling of the chamber back to the room temperature is the last step in the thermal shaping. The working differential pressure, once reached, is monitored and kept constant during entire cooling cycle. After completion, the differential pressure is brought back to atmospheric and lid removed. A frame, shown on Figure 16, is glued onto the already shaped Mylar film. The bottom surface of the frame has the required ellipsoidal shape. On the top there is a groove cut for a vacuum o-ring. In the figure several installed studs are shown in red. Figure 18 illustrates the gluing of the frame onto the pressurized thermally shaped Mylar. The largest portion of the Mylar, even while pressurized, is stress free. That portion of the surface which is in full contact with mold, is leaning on it and therefore no stresses are involved here. Only the unsupported deflected portion of Mylar that is out of the gluing frame is under the stress. After the glue is polymerized a flat Plexiglas lid is attached to the frame. Then the vacuum chamber is released. The deflected portion of Mylar provides stress relief. The Mylar film shaped at no residual stress together with frame and lid is cut out as a single unit for future use.

The other important component of the mirror is the mechanical support substrate, which is made of rigid foam. A sheet of polymer of certain size is sanded down, under its own weight,

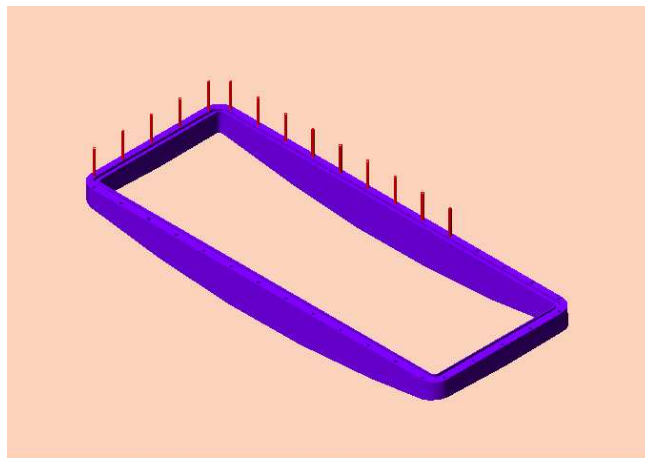


Figure 16: Gluing frame

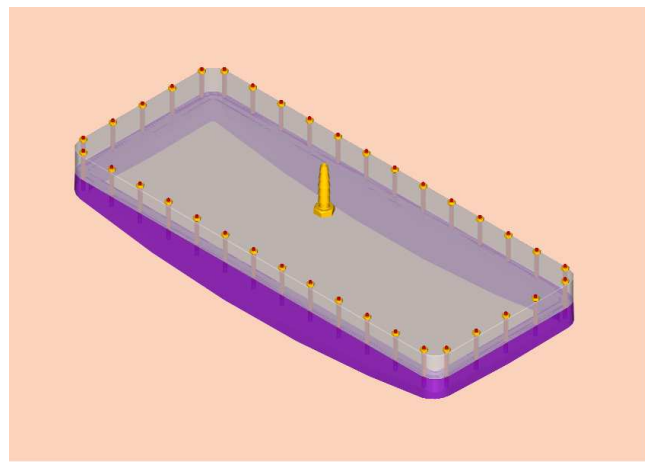


Figure 17: Gluing frame with plexiglas lid on the top, and Mylat attached to the bottom.

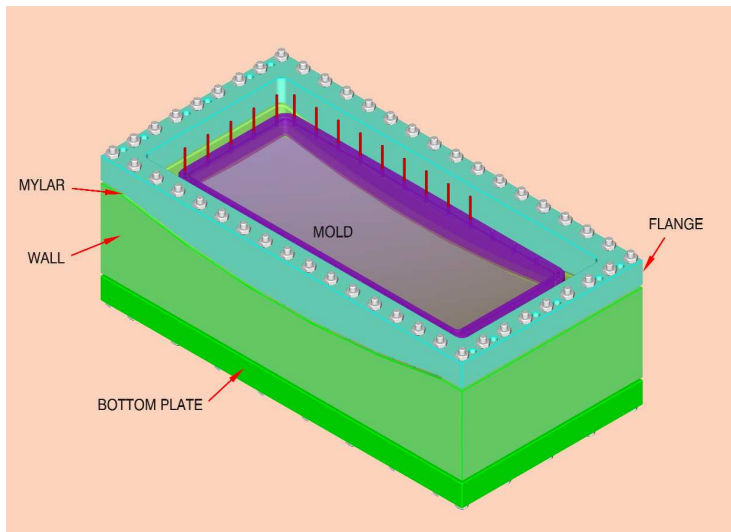


Figure 18: Frame glued onto thermally shaped Mylar film leaves Mylar stress free after chamber is depressurized.

until it providing a flat base. The top of the flat sheet is cut by CNC milling to the concave ellipsoidal shape, which mates to the back surface of the Mylar mirror substrate, as seen in Figure 19. The length and width are appropriate for gluing the frame and mold.

In order to process the front (working) surface, the substrate is mounted on an auxiliary table and glued to it along the edges at several locations, as shown in Figure 20. The top of the table and back of the substrate have exactly the same ellipsoidal shape, thus providing the required rigidity for further processing.

Figure 21 shows the cutting of the working surface to the shape of an ellipsoid. The ellipsoid parameters were defined by taking into account the thickness of the anticipated glue joint and of the thermally shaped Mylar film. The diameter of a ball end mill, regime of cutting and value of overlaying steps between consequent cuts were optimized to get surface finish smooth enough so that no polishing would be necessary. Due to the foam structure there were no scallops observed. In Figure 22 are shown sample pieces of thermally shaped Mylar films, the mold used in shaping them, and completely processed foam substrate mounted on the auxiliary table.

The final step in mirror construction is the gluing of the shaped Mylar onto the ellipsoidal substrate. The gluing frame, with transparent Plexiglas lid on the top, and the Mylar film attached to the bottom (see Figure 17) is pressurized at differential pressure up to $\sim 2 \times 10^{-2}$ Torr, so that the film bulges out beyond its normal convexity. Low viscosity degassed epoxy with extended polymerization time is uniformly applied to the ellipsoidal surface of the sub-



Figure 19: Substrate: flat face down, cylindrical top

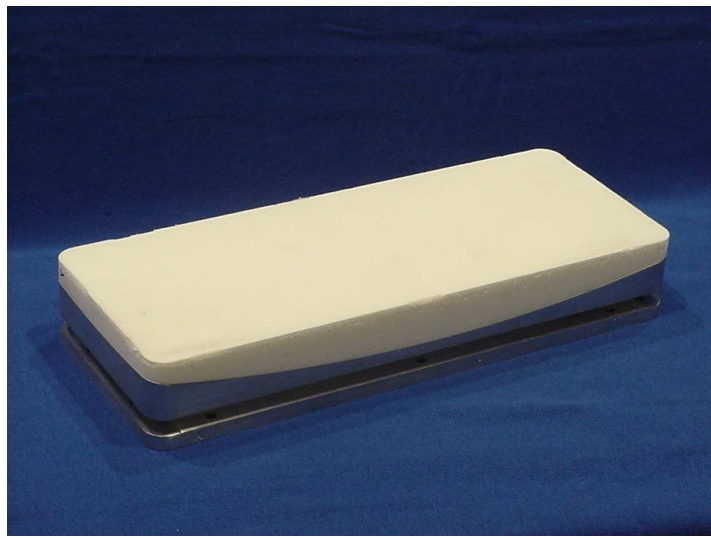


Figure 20: Substrate mounted on auxiliary table



Figure 21: Computer Controlled cutting of ellipsoidal surface of foam substrate

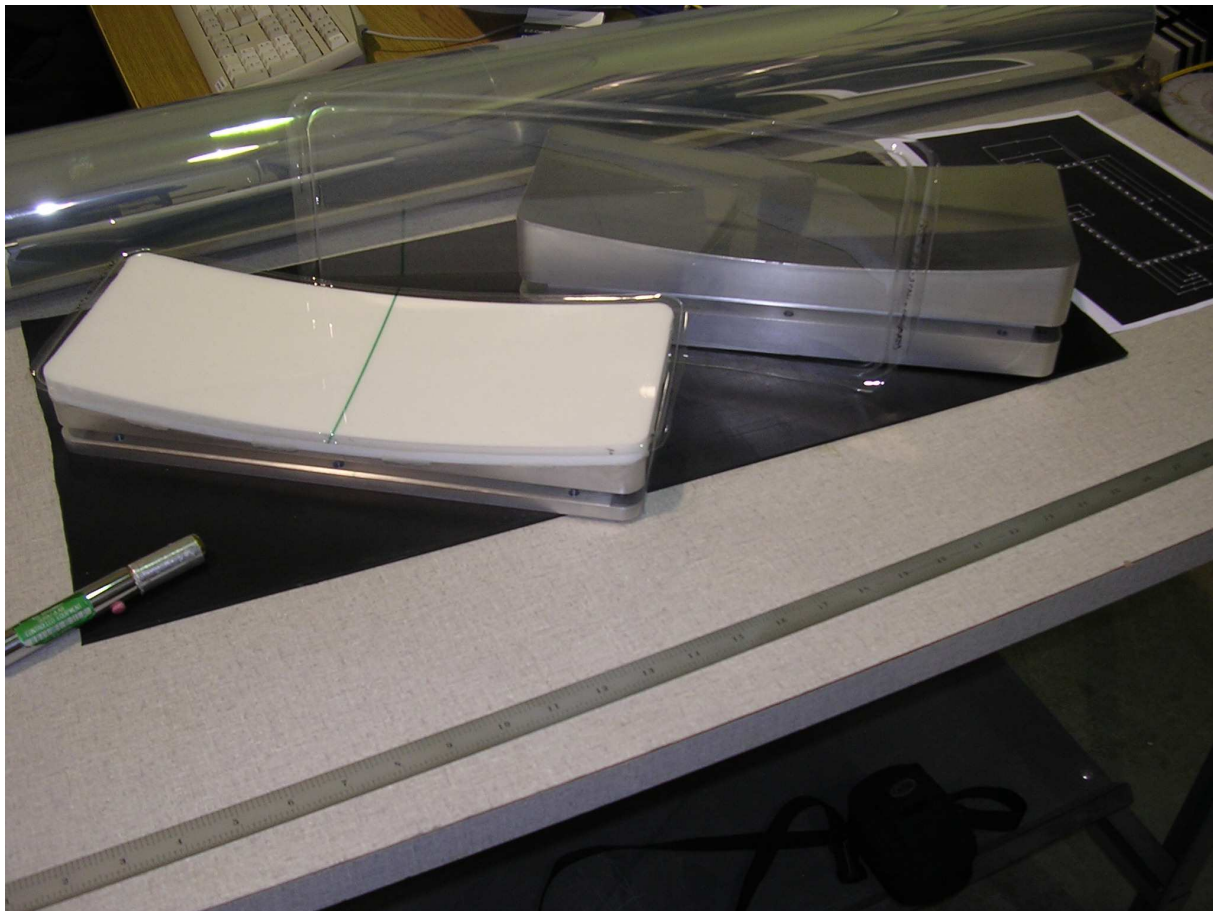


Figure 22: Substrate components and metal tooling used in construction of mirror prototype

strate which remains attached to the auxiliary table. Then the pressurized frame with bulged Mylar is placed on top of the substrate slowly enough to let trapped air bubbles escape. A transparent lid allows visual control of quality of the joint. The Mylar is fully pressed against the substrate, and stays under uniformly distributed pressure until the epoxy is cured. The position of the frame relative to the table is controlled. After curing the frame is depressurized, the lid removed, the auxiliary table with its components is placed back on the CC milling machine. The inner portion of the composite substrate is directly cut out through an opening on the frame. Measurements have shown that the total thickness of the composite substrate was $73\text{-}74 \text{ mg/cm}^2$. There is a potential of further decreasing a mirror's thickness without altering the technology described in this section. It would leave some contingency in varying mirror thickness within factor of ~ 2 while optimizing the overall rigidity.

In 2007 R&D is planned to check the last step of construction of the mirror consisting of three different ellipsoidal segments. A critical issue to be addressed is whether the estimated tolerances of assembly can be achieved.

Each of the three mirror segments, once built according to already established technology, is put on the modified auxiliary table with special grooves cut on top. Then all four sides (one at the time) are cut under particular angles (all different), defining the orientation of the planes along which ellipsoids intersect. The accuracy of cutting (including positioning) is limited typically by $\pm 0.001''$. Figure 23 shows a substrate which has been processed on all sides (in yellow) mounted on the modified auxiliary table. The sides of all segments are cut using their own table since the angles and dimensions are different for each. But, the back surfaces of all three segments, and the top of corresponding tables are cylindrical with the same parameters, so that the segments can be mounted next to each other on a larger table with top surface of cylindrical shape. This is illustrated in Figure 24. After alignment checks they will be glued together along the planes of intersection.

2.2 Light Collection Cones.

GEANT simulations of HTCC optics and performance show that for point like target with no magnetic field almost all Čerenkov photons are focused on photocathod of diameter 110mm, which is minimal for 5" PMTs from Photonis. In experiments with CLAS12 standard cryogenic targets are 50mm of length, and in some experiments targets as long as up to 100mm can be used. For all experiments with electron beam the superconductive solenoid and the Čerenkov counters will be used. As it was mentioned in section 1.1, to have efficient Čerenkov light

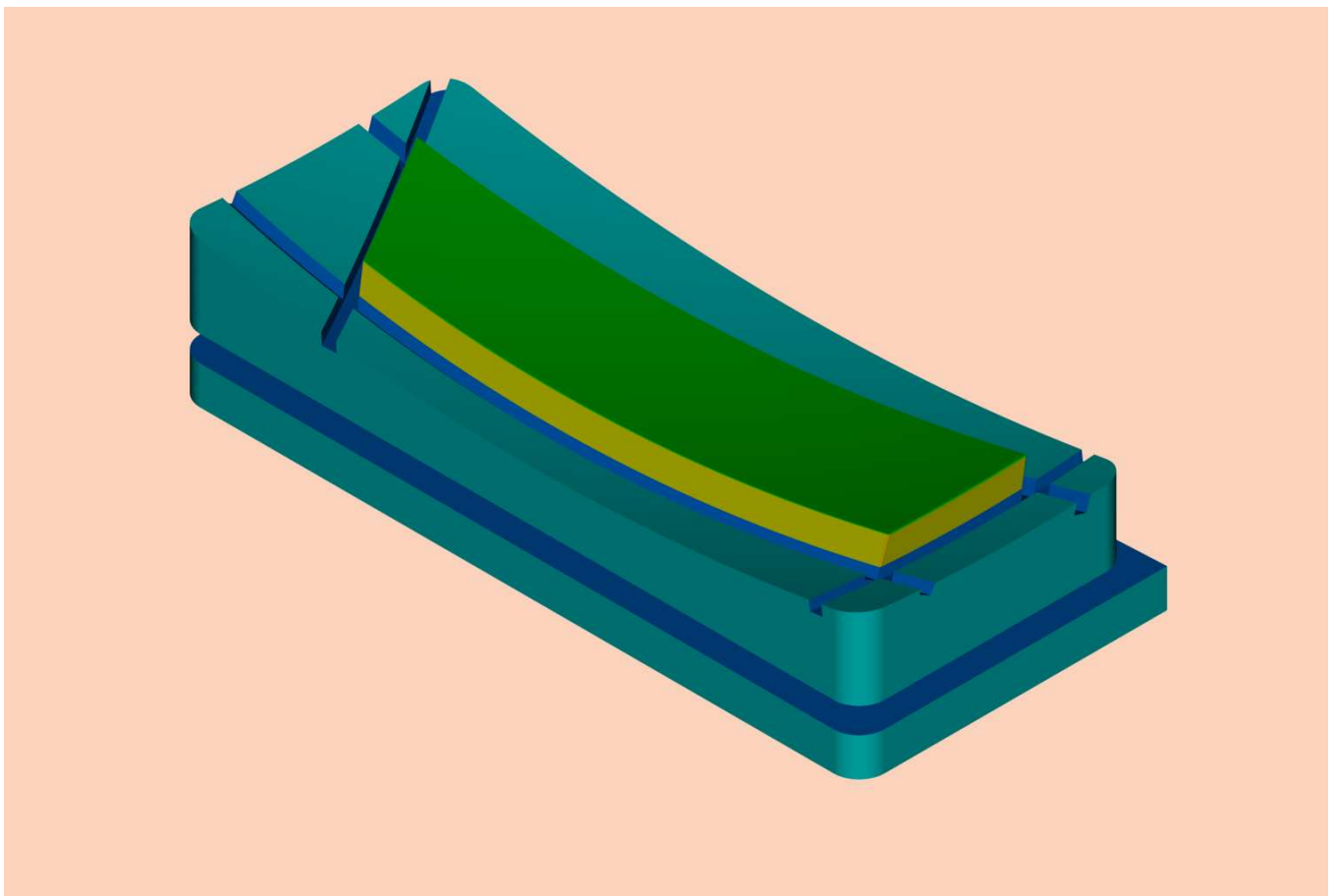


Figure 23: Completely cut maunted on the modified auxiliary table

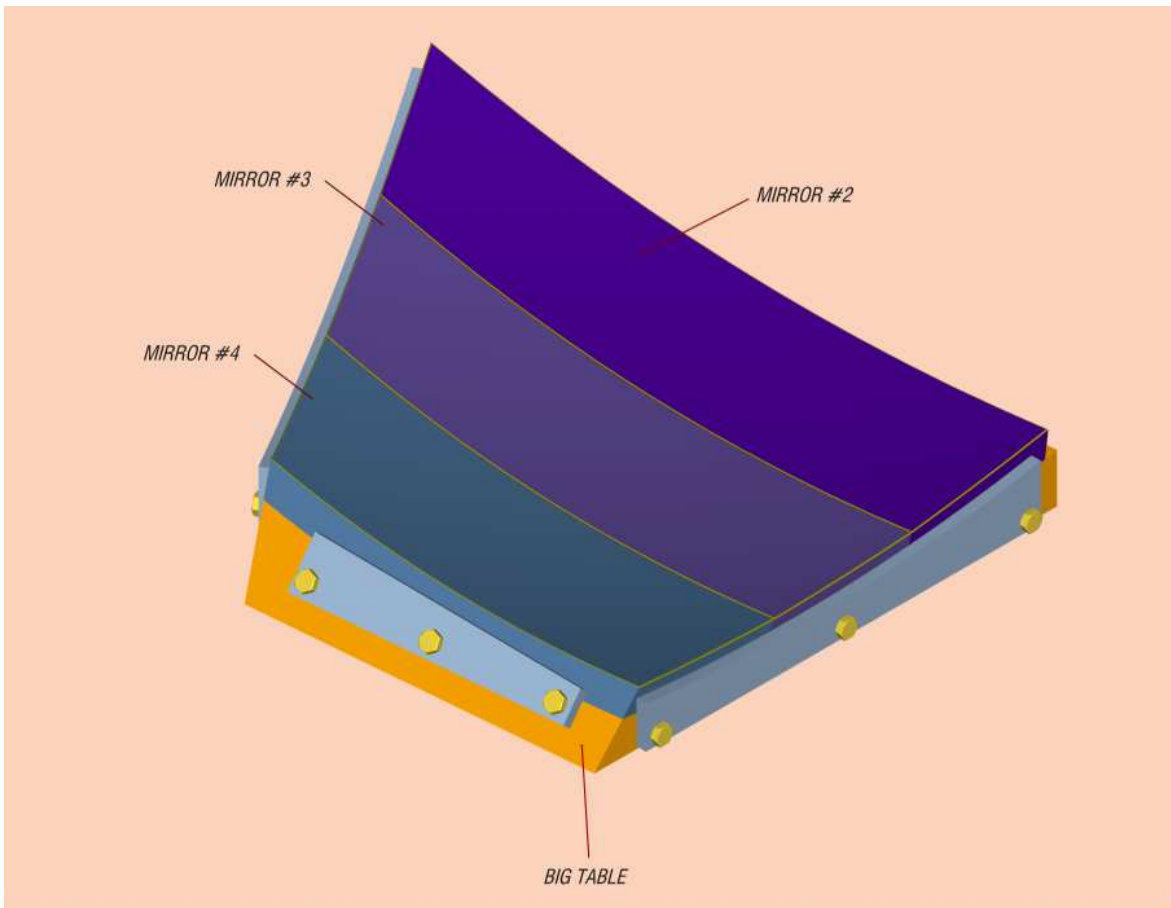


Figure 24: Mirror segments mounted on big table. Left and right sides of mirrors are planes along which will be glued adjacent similar mirror assembly.

Table 1: Specifications for HTCC Winston Cones for CLAS12 spectrometer

SPECIFICATION	DATE	SOURCE
Winston Cone Definition		
A Winston Cone is a non-imaging light collector designed to collect light from a range of incident angles on a given circular area and collect that light onto a smaller area. The Winston Cone is not a focusing device, but it is highly efficient in collecting light. Its general, the shape is that of a parabola that revolves about the axis of symmetry of the parabola.		
BASIC		
Material = copper outer surface with inner coatings of nickel, aluminum, and magnesium fluoride (see below)	12/2006	P. Stoler
Weight = 4 lbs (approximately)	12/2006	Y. Sharabian
Life time = 30 years with no optical degradation	12/2006	P. Stoler
Dimensions = $\phi 7.5'' \times 8.0''$ long	12/2006	Y. Sharabian
Optical and structural properties tolerant to high radiation dose 20 Megarad/20 years	09/1991	C. Zorn
Most radiation is in x-ray region, some relativistic particles	05/1992	C. Zorn
MANUFACTURING		

collection for extended targets in magnetic fields light collection cones are necessary. To define main parameters for the Winston Cones we required an opening diameter of 7.5" and distance from PMT photocathode to be equal 8" allowing magnetic shields be extended far enough beyond photocathode. Direct comparison of such Winston Cone angular acceptance with results of Monte Carlo simulations showed that the Winston Cones acceptance is much wider, and the opening diameter is big enough to collect at least 95% of Čerenkov light in experiments with two possible polarities of the CLAS12 Torus Magnet without any adjustments of PMTs location or orientation.

There are well established and experimentally checked technologies for constructing Winston Cones. Such light concentrators were built for the existing Low Threshold Čerenkov Counter of CLAS by electroforming technology and have shown sustained undiminished performance for more than a decade. The technical specifications and requirements of the proposed Winston Cone for the HTCC, similar of those used in CLAS, are given in Table 1. The corresponding parameters are given in Figure 25.

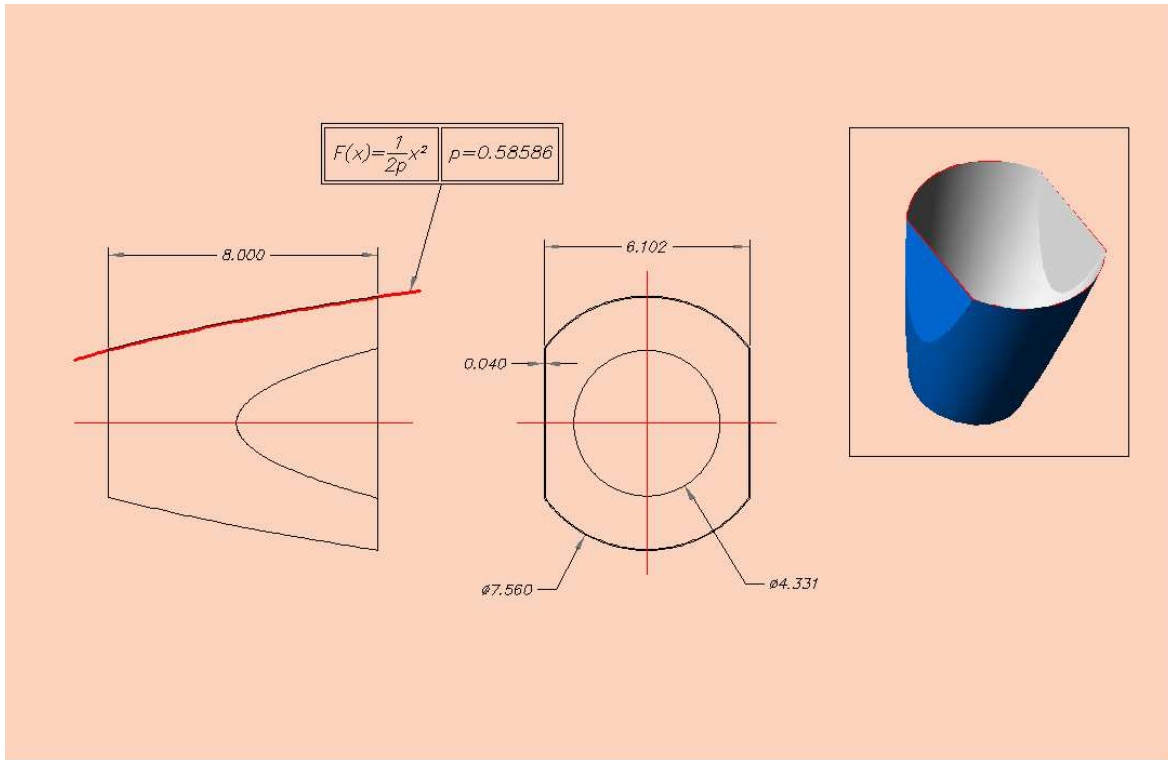


Figure 25: Winston Cone for HTCC

Table 1: Specifications for HTCC Winston Cones for CLAS12 spectrometer (continue)

3 DAQ for HTCC

Signals from Cherenkov Counter will be used in generation of trigger and for timing purposes as well. Photomultiplier tube will supply anode signal over coaxial cable to a passive splitter installed on Forward Carriage. One of the output signals from Splitter will go to Flash ADC (see Figure 26) and the other one to Timing Discriminator, connected to Pipeline TDC.

Flash ADC will have 12 bit resolution and 250MHz clock. Pipeline TDC will provide 85psec time resolution. Timing Discriminators will have build-in scalers for each channel.

Sums from Flash ADCs will be delivered to Trigger Processing Boards and used to generate Level-1 trigger along with other fast detectors of CLAS12. The mirror segmentation in polar angle allow as use a HTCC for selecting angle ranges at level 1.

Slope errors < 1°	12/2006	D. Kashy
Surface finish of Root Mean Square = 0.5 μm (microns)	12/2006	Y. Sharabian
Scratches occurring in forming operation etc. need not be removed provided in the final product there are less than 4/cone and 1) they are less than 2.54 cm in length 2) they are less than 0.15 μm (microns) deep Open Ends flat within 0.03"	12/2006	Y. Sharabian
OPTICS	12/2006	Y. Sharabian
MATERIAL	12/2006	P. Stoler
Copper: Thickness = 0.040" nominal Application method = electroformed None-magnetic		
Nickel: Thickness = 0.0005" nominal Application method = electroformed Allowable magnetic properties		
Aluminum: Thickness \approx 0.04 μm (microns) Application method = vacuum (vapor) deposition None-magnetic		
Magnesium fluoride (protective coating) Thickness = as required to meet reflectivity specifications Application method = vacuum (vapor) deposition None-magnetic		
ENVIRONMENTAL	12/2006	Y. Sharabian
Operating CO ₂ at 1.001 atmosphere, temperature = 22° C Stored in plastic bag w/ambient air to avoid dust contamination DO NOT contact reflective surface with anything Wash reflective surface w/only optical liquid (Check this spec)		

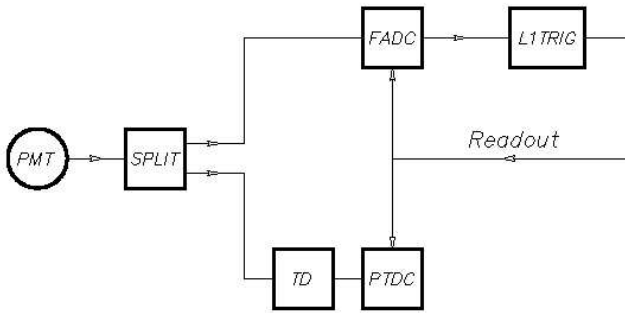


Figure 26: Single channel scheme of readout for HTCC

4 HTCC Gas System Overview

The CLAS gas supply system for existing Low Threshold Cherenkov Counter will be used for HTCC as well with minor upgrades of two reserved lines. Gas is supplied via CO₂ Dewar boil off of Coleman grade gas, 99.98% minimum purity. Pressure is reduced in 3 stages. Dewar output is set to 175 psig, house line regulator is set to 35 psig, and hall supply is set to 15 psig.

A continuous flow of gas, CO₂, is supplied to the detector via an MKS Mass Flow Controller (see Figure 27).

The pressure in the detector is controlled by pumping the gas out of the detector via a pump and an MKS proportional control valve. An MKS pressure controller adjusts the valve position to maintain 0.05"wc pressure in the detector. Both supply and exhaust systems fail safe on loss of power and required manual restart when power is restored.

Both ACTIVE and PASSIVE over-pressure and under-pressure protections for the detectors are used. Active protection uses an OMEGA process controller to operate solenoid isolation valves. One valve isolates the detector from the gas supply to prevent an over-pressure condition. The other solenoid isolates the detector from the exhaust manifold to prevent an under-pressure condition. These solenoid valves also isolate the detectors in case of power failure. The active level automatically provides action to mitigate the pressure problem. Passive protection uses oil filled bubblers which are installed on the detector itself. If the differential pressure inside the detector exceeds 0.125"wc, gas will either vent to atmosphere or be sucked into the detector to prevent damage. Bubblers are sized such that they can vent full gas system supply or exhaust flow in case both the pressure control system and active

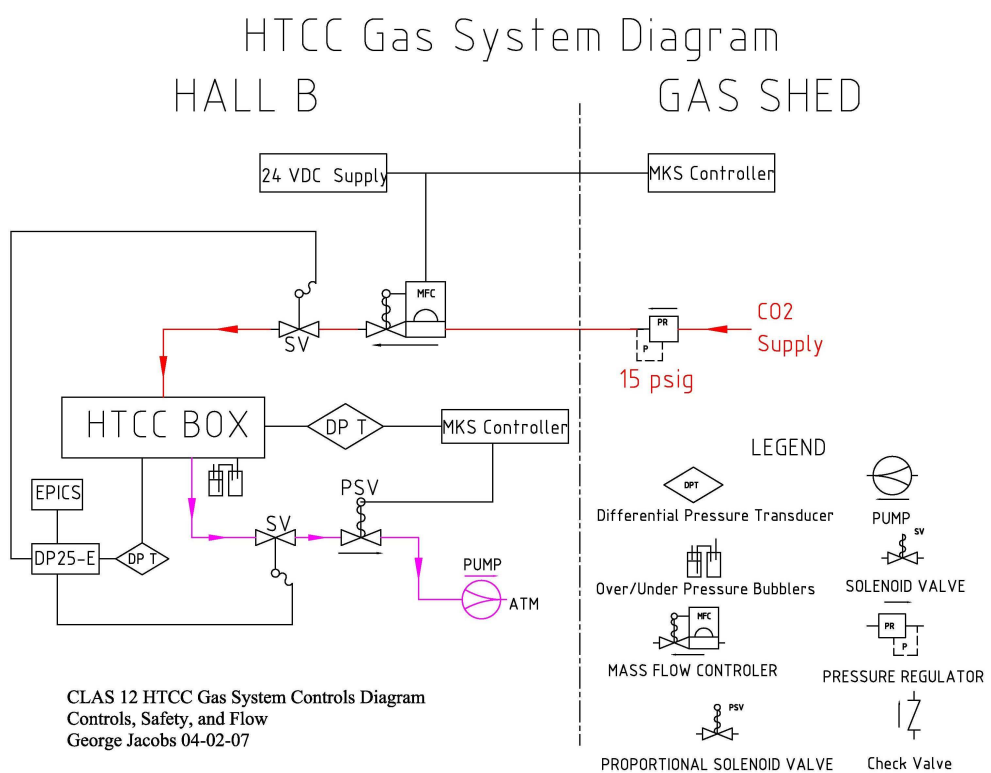


Figure 27: HTCC Gas System diagram

safety systems fail.

5 Simulations of Detector Performance

Extensive Monte Carlo simulations were carried out as part of the detector design procedures. This section describes some of the features of the expected detector performance based on the current design.

5.1 Optical Properties of physical components

The criterion for the choice of physical components is to maximize the production and detection of electron Cerenkov light with the maximum threshold energy for pion Cerenkov radiation. Figure 28 is a composite showing the properties of the various materials which play important roles in Cerenkov performance.

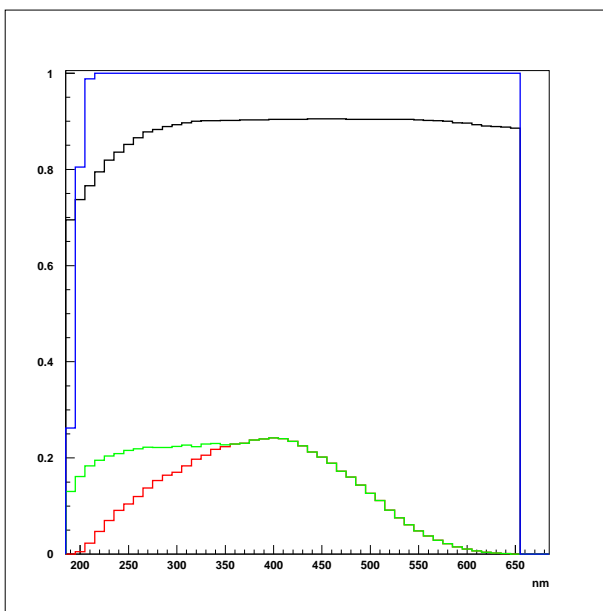


Figure 28: The optical properties of components of the HTCC relative to maximizing the number of detected photoelectrons as a function of photon wavelength. The transparency of CO₂ is shown in blue, the reflectivity of aluminum in black, the photo efficiency of a PMT with a UV glass window in red, and a quartz window in green.

5.1.1 Radiator Gas

The choice of radiating gas is CO₂, which has excellent optical transparency for wavelengths as low as 200 nm (see Figure 28). This is an important feature since the spectrum of Cerenkov light is approximately $dn/d\lambda \propto 1/\lambda^2$. The low index of refraction, $n \sim 1.0041$, corresponds to a pion threshold energy of 4.7 GeV²/c². A tradeoff is that fewer photons are produced at such low values of n . However, as will be seen, the number of collected photons is high enough to ensure a high detection frequency.

5.1.2 Photomultiplier Tubes (PMT)

The use of 5-inch Photomultiplier tubes was chosen as the best match for the optical properties of the HTCC. This will be clear in the section on the photon spacial distributions at the face of the PMTs. After consideration of PMTs from several manufacturers ¹, the Photonis XP4508 was chosen to have the best overall characteristics for our requirements. The window material is an important consideration. Figure 28 compares the quantum efficiency of the Photonis XP4508 with UV glass and quartz windows. Clearly, the quartz window is superior in the low wavelength regime in which there are a large number of photons and matches the transparency range of the CO₂, as well as the reflectivity of the Al-MgFl mirror surfaces, which are also shown in Figure 28. The shape of the PMT surface has also been considered, since the reflectivity of the PMT window, and thus the quantum efficiency, depends on the distribution of angles of photons relative to the PMT surface. Figure 29 shows the simulated distribution of photon angles relative to the normal to the PMT surface for convex and flat windows respectively. It is seen that the distribution for the flat surface is closer to the surface normal than for the convex surface, and thus the flat surface quartz window was chosen as most appropriate for our purposes.

5.2 Distributions of Photons incident on the PMT faces.

Simulations were carried out to assess the HTCC response to scattered electrons as a function scattering angle in both θ and ϕ . The results discussed in this section are for electrons of energy 2 GeV uniformly distributed in $d\Omega = \cos(\theta)d\theta d\phi$. Each mirror is designed to direct the Cerenkov light which impinges upon it onto the face of a specific PMT. Figure 30 shows the distribution of electrons reaching PMTs 1,3,5 and 7, corresponding to mirrors reflecting

¹Electron Tubes, Burle, Hamamatsu, Photonis

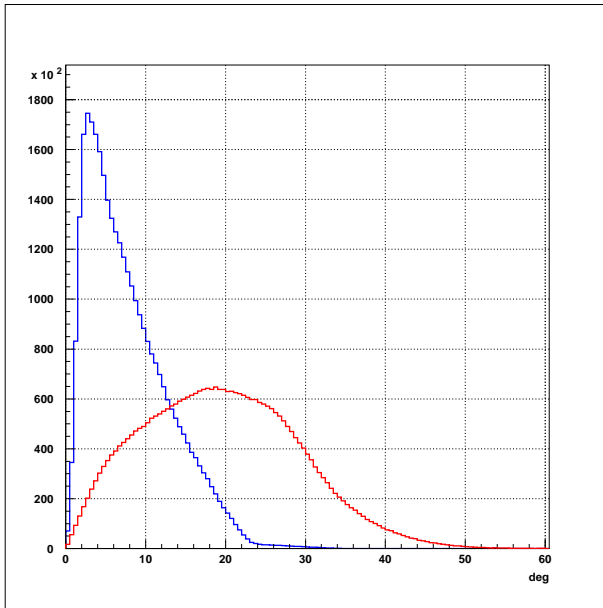


Figure 29: The simulated distribution of photon angles relative to the normal to the PMT surface for convex (red) and flat (blue) windows respectively.

light from electron scattering angle θ approximately 9° , 16° , 23° and 30° , respectively. The electrons originate from a target of length 10 cm which is centered at the nominal central target position, with the full magnetic field configuration. It is observed that the photons are constrained to circles of diameter approximately 16 cm, which is somewhat larger than the 11 cm PMT active diameters. Thus, light collection cones (Winston Cones) have been designed to redirect the photons which arrive outside of the photosensitive areas of the PMTs into the photosensitive areas.

Figure 31 shows the overall acceptance in number of photoelectrons as a function of θ and ϕ for one half of a sector, corresponding to the *standard* conditions described above. The results are the same for the 12 symmetrically placed half sectors corresponding to a full $\Delta\phi = 2\pi$. Figure 32 are the projections of Fig. 31 vs. θ and π respectively. One observes that the mean number of photoelectrons is greater than 10 in scattered electrons in the angular range from about 5° to 40° .

The effect of the fields and target location on the performance of the detector are illustrated in Figure 33 a,b,c and d, which show the distribution of photons on one PMT, number 4. The target is 10 cm long located at the central detector position, with no magnetic field (a) and with full magnetic field (c). Also shown in (b) and (d) are the equivalent distributions for the target displaced 10 cm downstream respectively. One observes that the radii of the

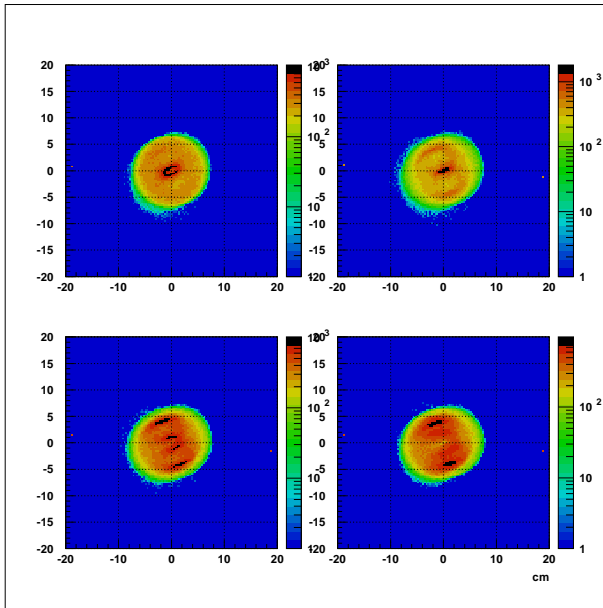


Figure 30: The distribution of electrons reaching PMTs 1,3,5 and 7, corresponding to mirrors reflecting light from electron scattering angle θ approximately 9° , 16° , 23° and 30° , respectively

distributions do not vary greatly under the four conditions shown. This is true for the other PMTs as well. Figure 34, shows the mean square radius for the photon distributions under the four conditions indicated above for all eight PMTs.

5.3 Background Rates

Figure 35 illustrates the background rates due to various secondary electrons and positrons which result from primary particles colliding with the materials of the detector. The maximum rate, about 10 kHz, occurs in the tubes corresponding to the smallest angles. These rates are small enough to be easily handled by the data acquisition system.

As a final example we present in Fig. 36 the simulated ratio of pions to electron identification for 4 MeV pions and 2 GeV electrons. This rejection ratio varies between 2 and 6×10^{-3} . Note that at back angles very few pions will be produced at such high energies, while lower energy pions will be rejected with much greater efficiency.

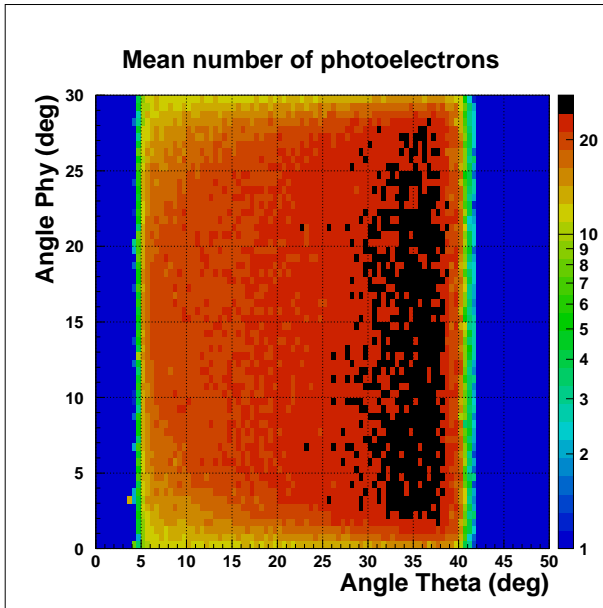


Figure 31: The overall acceptance in number of photoelectrons as a function of θ and ϕ for one half of a sector.

6 PMT Studies

6.1 PMT magnetic shielding studies

The PMT of the Čerenkov counter will be located in a region in which there will be a significant magnetic field, primarily from the solenoidal magnet which surrounds the target and central detector system. The field varies considerably with distance from the solenoid, with a maximum value of as much as 50 Gauss in the region of the PMTs closest to the solenoid. To give an idea of the magnitude of the problem we note that for tests we have carried out, the PMT gain is reduced by a factor of two for a magnetic field of 0.4 Gauss perpendicular to the PMT axis and 1.3 Gauss parallel to the PMT axis. The standard PMT magnetic shield which can be obtained from the PMT manufacturer is totally inadequate to reduce the ambient field to even these levels, so that it is necessary to custom design a magnetic shielding system appropriate for the CLAS12 HTCC configuration. The design is being carried out with the aid of the TOSCA magnetic field program.

Figures 37,38,39,40 present the residual magnetic field at the PMT axis for standard one layer PMT magnetic shielding for three values of the magnetic field: 50, 40, and 30 Gauss with the direction of the magnetic field perpendicular and parallel the PMT axis (linear and logarithmic y scales are shown). In the first case the residual magnetic field inside the PMT

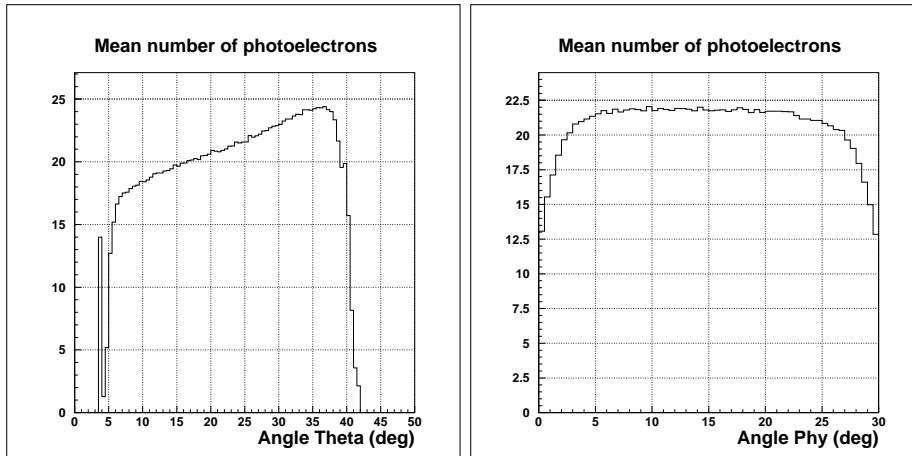


Figure 32: The projections of Fig. 31 vs. θ and π respectively.

volume is around 8, 2, and 1 Gauss for the magnetic field 50, 40, and 30 Gauss respectively. For the second case (the field is along the PMT axis) the field residual is significantly higher. The residual magnetic field inside the PMT volume is around 30, 10, and 1-2 Gauss for the magnetic field 50, 40, and 30 Gauss respectively. We may conclude from this calculation that

- We need additional magnetic shielding to suppress the residual magnetic field to the level of 0.5 Gauss.
- The residual field is significantly (several times) higher when the magnetic field is directed along the PMT axis.
- The shielding needs to extend beyond the PMT window for at least one PMT diameter.

We modeled three layer magnetic field shielding configurations using the TOSCA program. Fig. 41 shows the residual field for 3 different configurations with cylindrical PMT magnetic shielding with the magnetic field directed along the PMT axis.

- One layer tube made of co-netic μ metal (shown in black)
- Two layers made of NETIC and CO-NETIC μ -metals (shown in red)
- Three layers made of NETIC, CO-NETIC, and CO-NETIC μ metals (shown in blue)

The residual magnetic field with the three layer shielding is below 1 Gauss in the region \pm 5 cm, which is inside the specs for magnetic field parallel to the PMT axis. The perpendicular field will be several times lower as we can conclude from our calculations with standard PMT magnetic shielding.

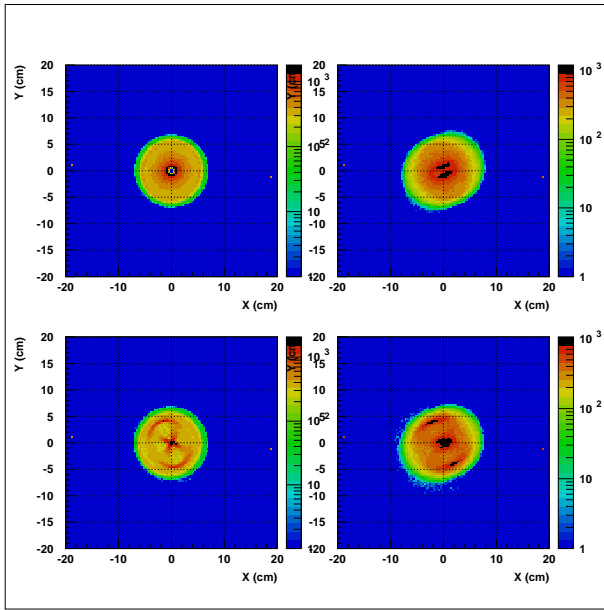


Figure 33: The effect of the magnetic fields and target location on the performance of the detector.

6.2 PMT Laboratory Studies.

There are two types of PMTs under investigation: those with UV-glass input window and those with quartz input window.

The UV-glass window features high quantum efficiency (22.5% at 385 nm) and ultraviolet response down to $\lambda \sim 220$ nm. The number of photons from the Čerenkov light is proportional to $1/\lambda^2$, so it's important to have an extended response in the UV wavelength region. The quartz window is transparent down to $\lambda \sim 180$ nm, which makes it more efficient for the detection of the Čerenkov light. However the PMT with the quartz window is much more expensive.

An experimental set-up was designed to measure the ratio of the average number of photoelectrons collected by these two types PMT's illuminated by Čerenkov light. Two methods are being utilized to measure this ratio.

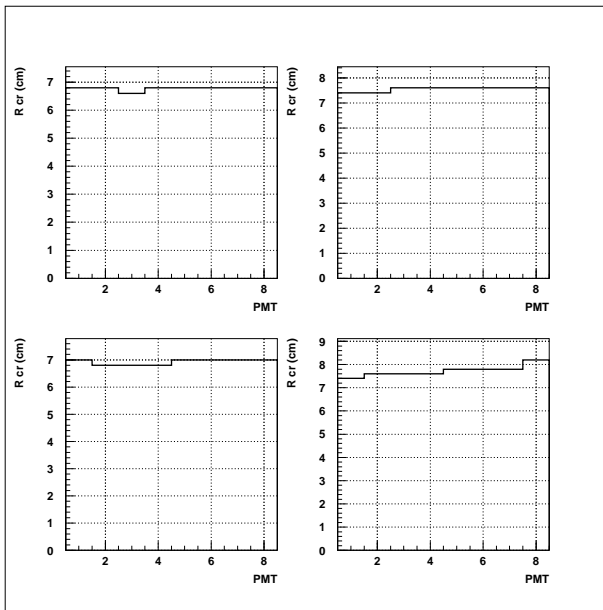


Figure 34: The mean square radius for the photon distributions under the four conditions indicated in the text for all eight PMTs.

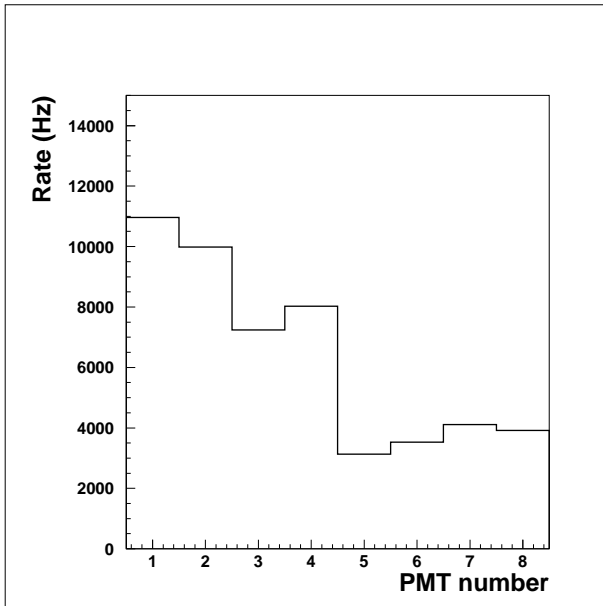


Figure 35: The background rates due to various secondary electrons and positrons which result from primary particles colliding with the materials of the detector.

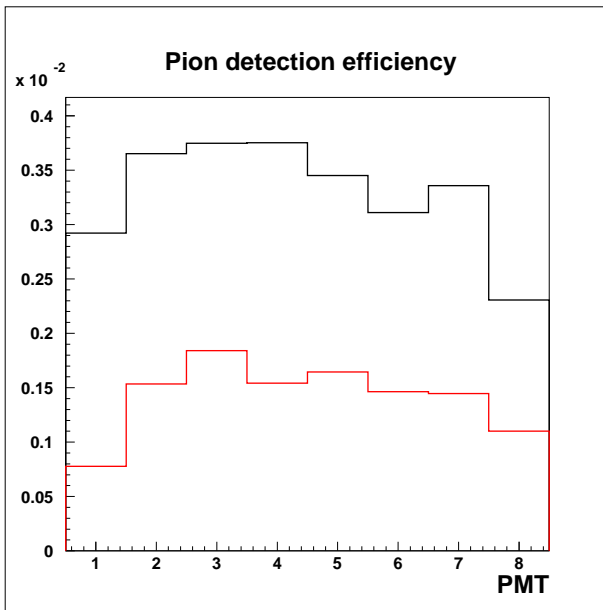


Figure 36: The simulated ratio of pions to electron identification for 4 GeV (black curve) pions and 2 GeV (red curve) electrons.

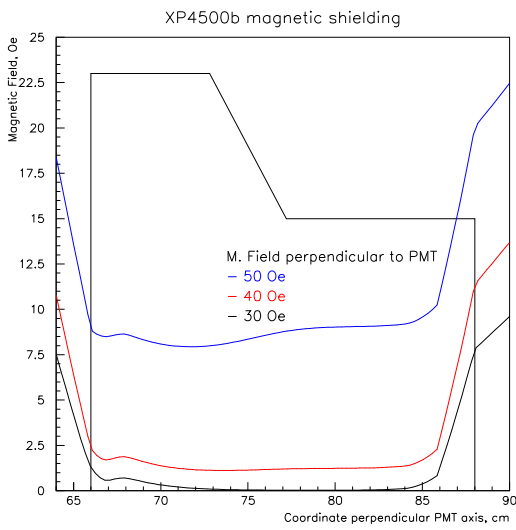


Figure 37: Standard one layer PMT magnetic shielding (shown in black). Magnetic field perpendicular to the PMT axis. The result with applied external fields of 50 Gauss field is shown in blue, 40 Gauss in red, and 30 Gauss in black.

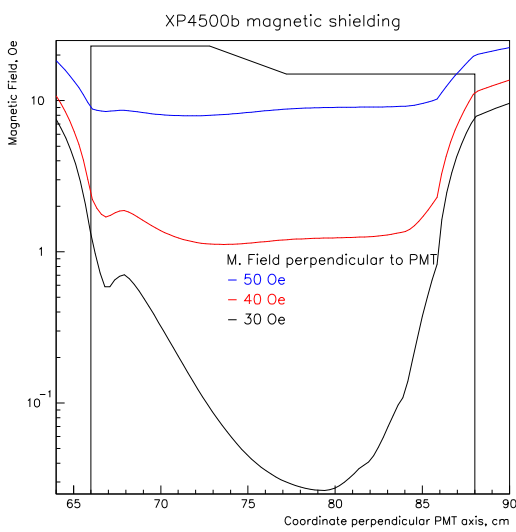


Figure 38: Same as in Fig. 37 but with a logarithmic y axis.

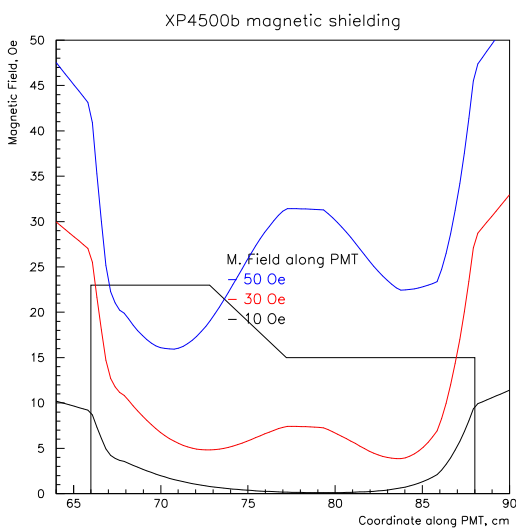


Figure 39: Standard one layer PMT magnetic shielding (shown in black). Applied magnetic field along the PMT axis: 50 Gauss is shown in blue, 40 Gauss in red, and 30 Gauss in black.

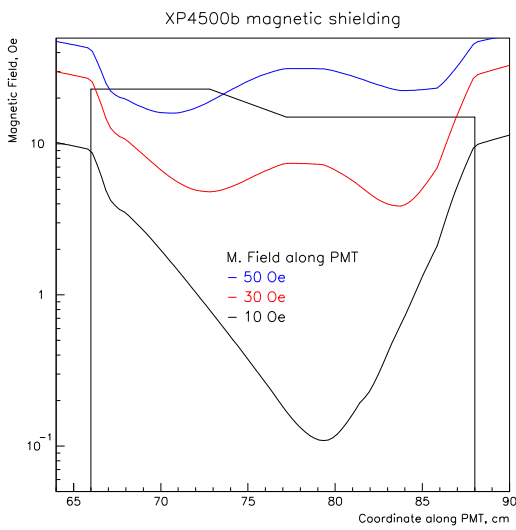


Figure 40: Same as Fig. 39 but with logarithmic y axis.

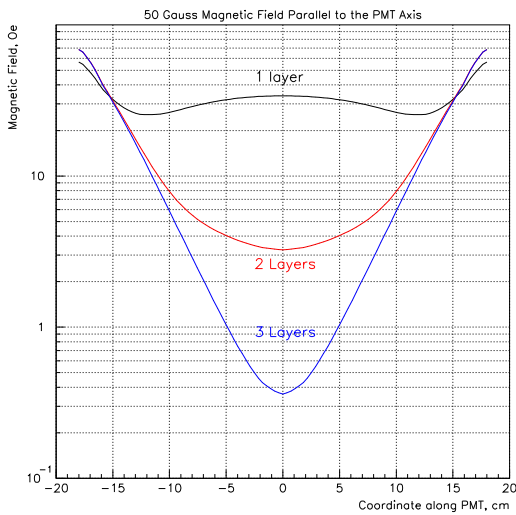


Figure 41: The effect of cylindrical PMT magnetic shielding, in which the applied magnetic field is 20 Gauss along the PMT axis. One layer shielding is shown in black. Two layers shielding is shown in red. Three layers shielding is shown in blue.

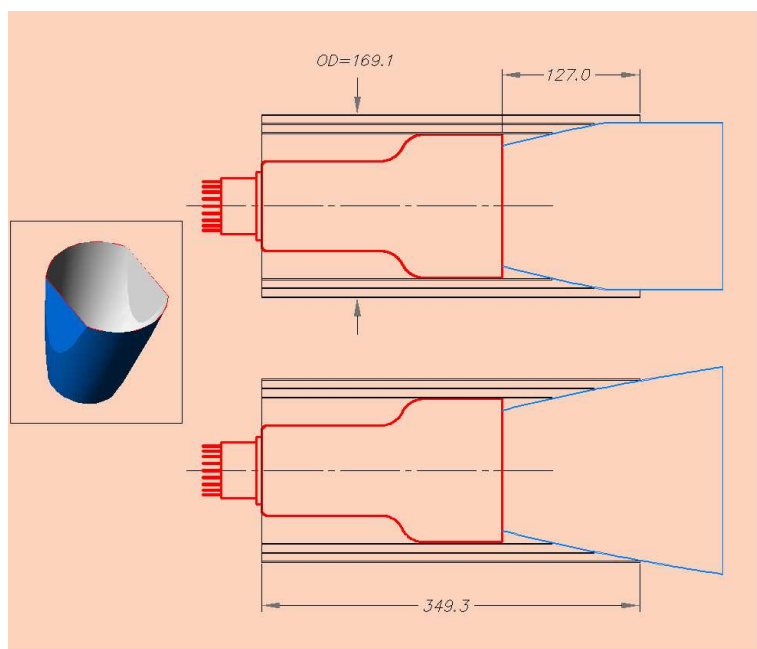


Figure 42: Assembly of Photomultiplier Tube with Winstone Cone Magnetic Shields.

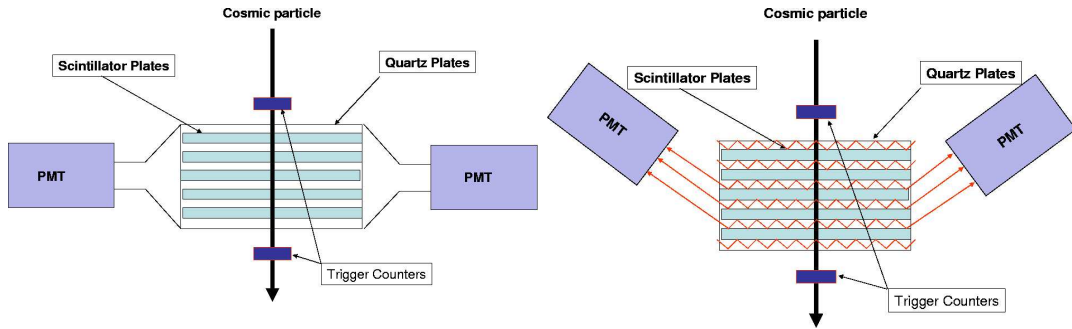


Figure 43: Left panel: view of the cosmic ray test stand from the side of the Čerenkov counters. Right panel: view of the cosmic ray stand from the side of the scintillation counters.

6.2.1 Cosmic Ray PMT Testing Apparatus.

Cosmic Ray Stand (CRS) was constructed in which the Čerenkov light is due to cosmic muons. The final goal is to compare the response of PMT with UV-glass and quartz input window to Čerenkov light. The test detector (Fig. 43) consists of alternate layers of scintillator and quartz plates of dimensions 150x150x5 mm. The Čerenkov light is produced in the quartz plates when irradiated with the cosmic muons. The light is directed to the photomultiplier tubes which are being tested, and their responses electronically analyzed. During the data taking data is accumulating for all tubes, and selections are made based on the results. Two 5x5 cm² trigger counters produce trigger signals that go to the data acquisition system. The signal from all 6 PMTs: trigger counters, scintillator counters and Čerenkov counters go to Amplitude to Digital Converters (ADC) for further analysis. Fig. 45 shows the ADC distributions.

The detector has three main subsystems.

- Trigger Counters MM1 and MM2. These counters are used to produce the trigger signal when cosmic muons cross the detector. The size of the trigger counters is small enough in comparison with the size of the scintillator and quartz plates to reduce the fluctuation of the produced Čerenkov photons due to edge effects.
- Scintillator Counters SC1 and SC2 collect light from the scintillator plates. These counters serve as an additional proof that cosmic muon cross the detector sandwich. Events with bad ADC signal in the scintillator counters are cut out.
- Čerenkov Counters CC1 and CC2. These counters collect the light from the quartz

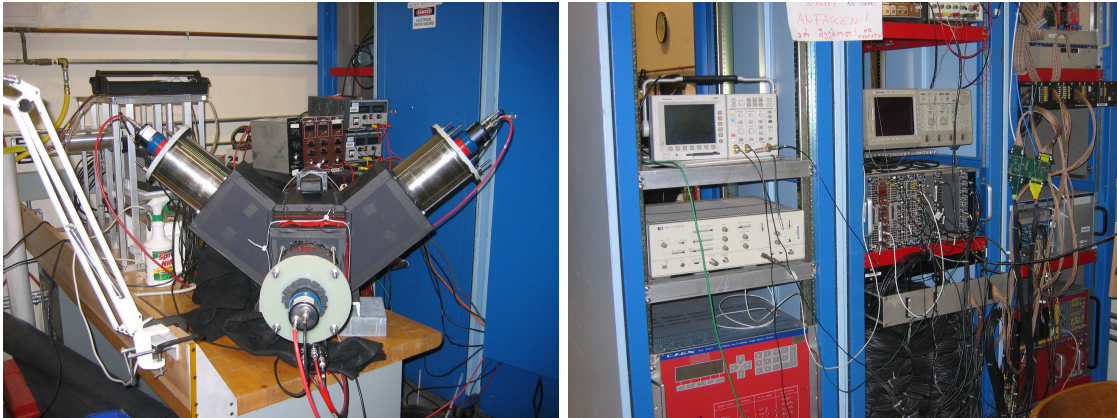


Figure 44: Left panel: photo of the cosmic ray stand. Right panel: photo of the data acquisition setup of the cosmic ray stand.

plates. One of the counters (CC2) serve as reference device. The CC1 position is used to study the PMT's.

The upper panels of Fig. 45 show the ADC distributions for the trigger counters for the events with amplitude in the scintillator counters (middle panels) more than 1000 counts. Clear signals for the cosmic muons are seen in both trigger counters. The events with lower amplitudes correspond to the case when the particle crosses the light guide.

The middle panels show the ADC distributions for the scintillator counters for the events with amplitude in the trigger counters (top panels) more than 800 counts. Clear signals from the cosmic particles are seen in both counters with good photo-statistics.

The bottom panels show the ADC distributions for the Čerenkov counters for the events with amplitude in the trigger counters (top panels) more than 800 counts. Clear signals from the cosmic muons are seen in both counters.

The even selection criteria are:

$$ADC(MM1) > 800, ADC(MM2) > 800$$

$$ADC(SC1) > 1000, ADC(SC2) > 1000$$

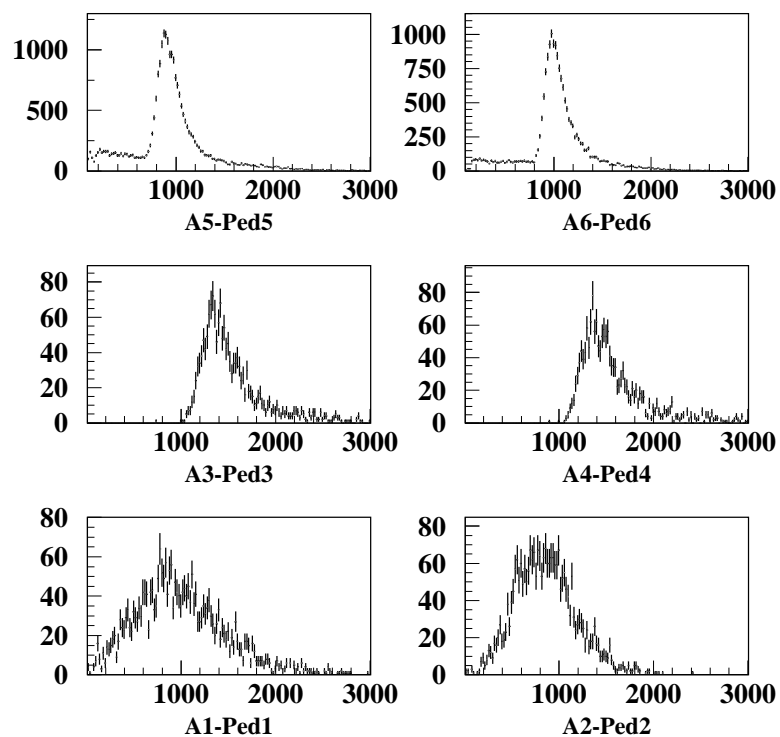


Figure 45: The ADC spectra for the trigger counters, scintillator counters and Čerenkov counters.

6.3 Calibration of the ADC scale

The ADC spectrum needs to be calibrated in the terms of photoelectrons for the PMT comparison. Two independent methods are used for this task.

The first calibration method uses the position of the one-photoelectron peak from real data. Fig. 46 shows the ADC distributions of the Čerenkov counter in the region near the pedestal. (The PMT was eliminated with light emission diode (LED) at low intensity). The peak near the pedestal corresponds to the one-photoelectron signal.

The second method uses a light emission diodes signal to calibrate the scale. PMTs were eliminated with the light of LED with variable intensity. The ADC spectrum was fitted using a Poisson function with two parameters.

$$N(x) = \frac{N_0}{\mu_1} \frac{\mu^{x/\mu_1} e^{-\mu}}{\Gamma[x/\mu_1 + 1]}$$

where N_0 is total number of events, x is the ADC channel, μ_1 is the calibration scale (the one-photoelectron position in terms of ADC counts), μ is the average number of photoelectrons and Γ is the gamma function, given by

$$\Gamma(x) = \int_0^{\infty} t^{x-1} e^{-t} dt$$

The fit gives the calibration scale μ_1 and the average number of the photoelectrons μ in the distributions. Figures 47,48,49 show the ADC spectra for different amounts of LED light for 3 different PMT's.

Figures 50,51,52 show the dependence of the average ADC value as a function of the fitted number of photoelectrons for three different PMTs as a function of the ADC value. The linear dependence shows that this method is self-concerted in all three PMTs. These two methods give very close results.

The normalized spectrum is shown in Fig. 53. These are the final distributions that will be used for the PMT selection. The PMT with better quantum efficiency for the Čerenkov radiation picks up more photoelectrons.

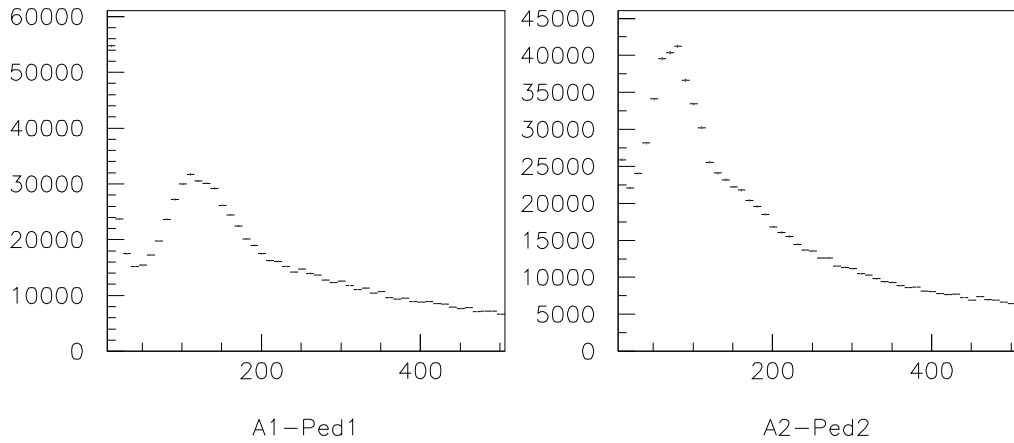


Figure 46: The ADC spectra of the Čerenkov counter. The one-photoelectron peak is clearly seen.

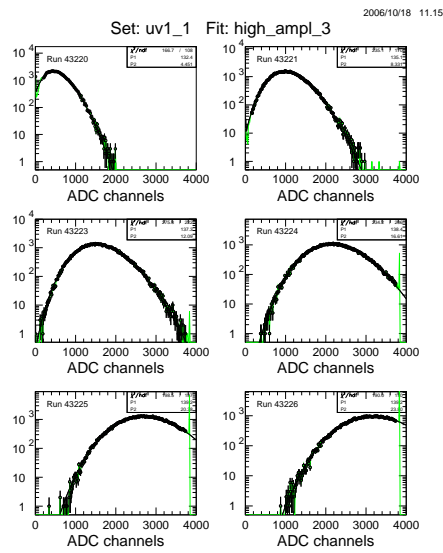


Figure 47: The LED spectrum of PMT N1. The spectrum was fit with Poisson function. P1 is the position of the one-photoelectron peak. P2 is the average number of the photoelectrons.

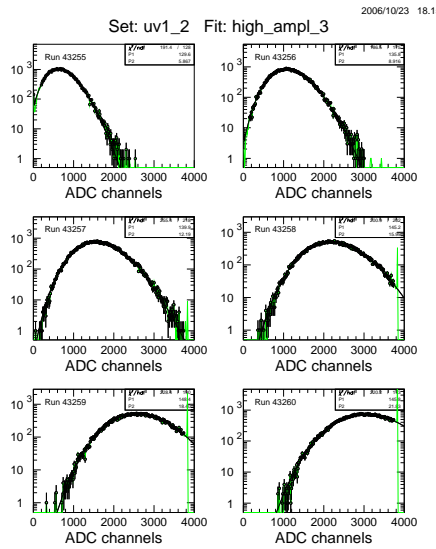


Figure 48: The LED spectrum of PMT N2. The spectrum was fit with a Poisson function. P1 is the position of the one-photoelectron peak. P2 is the average number of the photoelectrons.

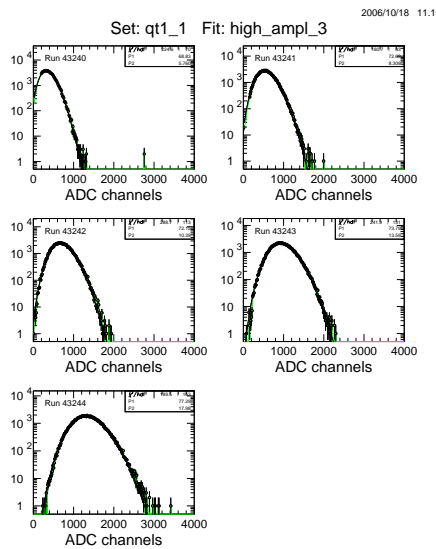


Figure 49: The LED spectrum of PMT N3. The spectrum was fit with a Poisson function with two parameters; P1 is the position of the one-photoelectron peak, P2 is the average number of the photoelectrons.

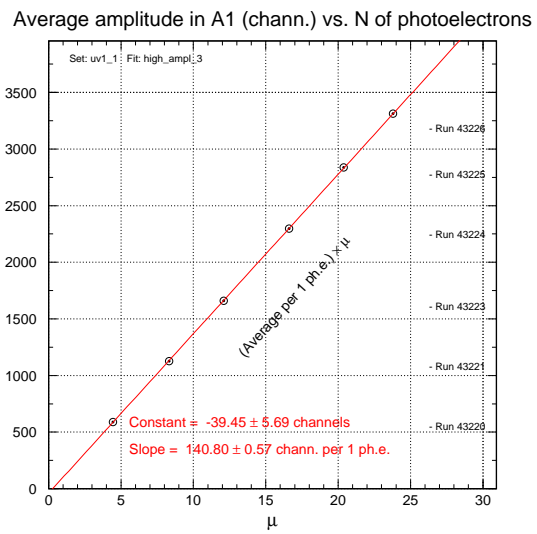


Figure 50: The ADC value vs fitted number of the photoelectrons for PMT N1. The fit is a straight line.

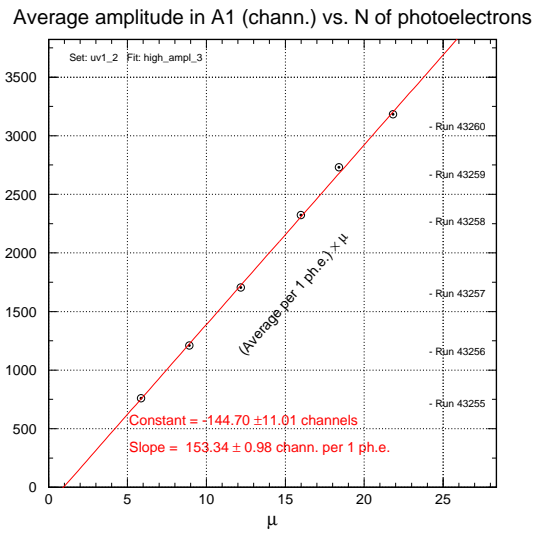


Figure 51: The ADC value vs fitted number of the photoelectrons for PMT N2. The fit is a straight line.

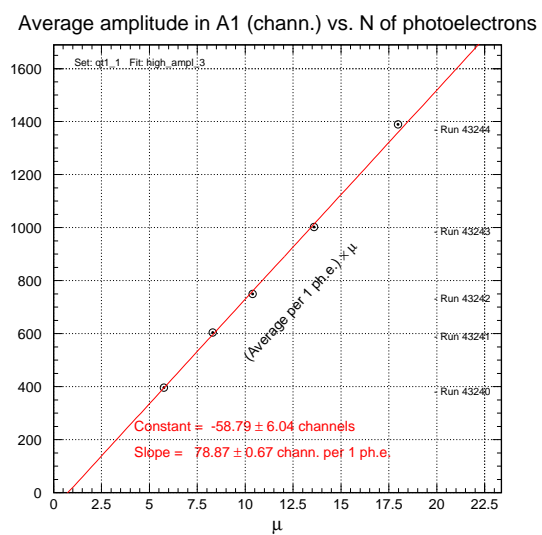


Figure 52: The ADC value vs fitted number of the photoelectrons for PMT N3. The fit is a straight line.

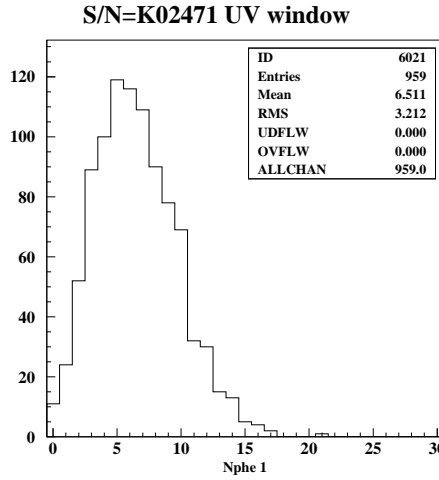


Figure 53: The distribution of the number of photoelectrons for the Čerenkov PMT with UV input window.

6.4 Relative Quantum Efficiency Measurements

The test stand to measure the relative quantum efficiency of different types of PMT's as a function of the wave length in the deep ultra-violent region is shown in Figure 54. The universal monochromator illuminator (Newport, model 7340) with Deuterium lamp is used as a source of high intensity ultraviolet radiation down to 160 nm. It is exactly what is needed for the PMTs with quartz or ultraviolet glass windows. The light source is directly connected with a CornerstoneTM 260 1/4 M monochromator (Newport, model 74100). It is designed for fast, automated scanning over a broad spectral range, even below 180 nm. The signals from the PMT is measured in the counting mode.

The PMT rate as a function of high voltage (HV) is shown in Figure 55. The plateau is clearly seen. The working HV is 2050 V for this particular PMT.

The top panel of Figure 56 presents the rate as a function of the light wave length for the PMT with quartz input window (shown in blue) and for the PMT with UV input window (shown in red). The bottom panel shows the ratio of these rates as a function of the wave length. It is clearly seen that PMT with quartz window begins to detect photons with wave length greater than 180 nm. At the same time the PMT with UV input window has a threshold near 220-240 nm. This is an extremely important consideration for the detection of Čerenkov light. The Čerenkov light spectrum behaves as $dN/d\lambda \sim 1/\lambda^2$. The ratio $R = \frac{N_{phe}^{Quartz}}{N_{phe}^{UV}} = 0.5$ at $\lambda = 230$ nm. We can estimate the ratio of the detected photoelectrons for these two type of PMT as

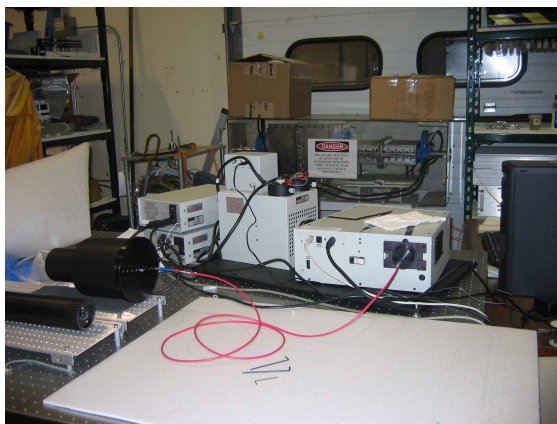


Figure 54: The stand for the optical test of the photomultipliers. The PMT in the black cylinder is connected by the fiber optics to the monochromator illuminator. The light source is a Deuterium lamp.

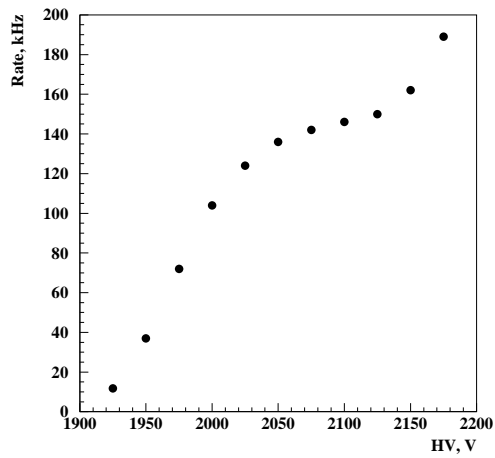


Figure 55: The PMT rate as a function of high voltage.

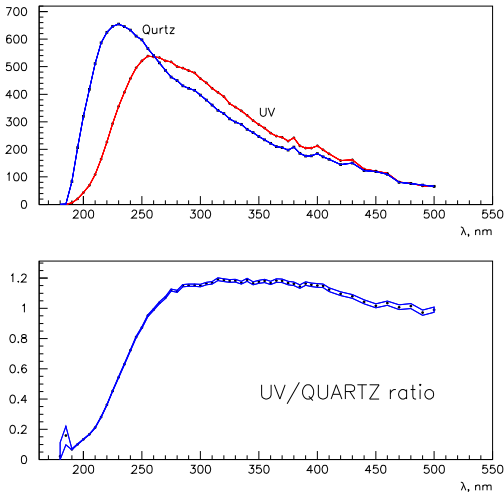


Figure 56: Top panel: the PMT rate as a function of the light wave length for the PMT with the quartz window (in blue) and with the UV-window (in red). Bottom panel: the ratio of these rates

$$R = \frac{N_{phe}^{Quartz}}{N_{phe}^{UV}} = \frac{\lambda_{threshold}^{UV}}{\lambda_{threshold}^{quartz}} \sim \frac{230}{180} \sim 1.3$$

This is close to the expected increase of the detected number of photoelectrons for the quartz PMT in comparison with the UV PMT.

7 Mechanical Design

The basic shape of the HTCC is naturally generated by a combination of the dimensions and positions of surrounding equipment, certain required acceptance angles, and the planned focal points of the mirror within. The body will serve primarily as a gas volume container, and should have as little material as possible within to obstruct either the Cherenkov light, or particles to other detectors. An overall view of the appearance of the HTCC, including its mechanical housing is shown in Fig. 57

7.1 Outer body

The mirror's design (six radial segments of two rows of eight mirrors) dictates a cylindrical ore hexagonal shell centered around the beamline, with a place on each segment to mount two rows of eight PMT's. The shape is simple, and can easily be constructed of flat, machined

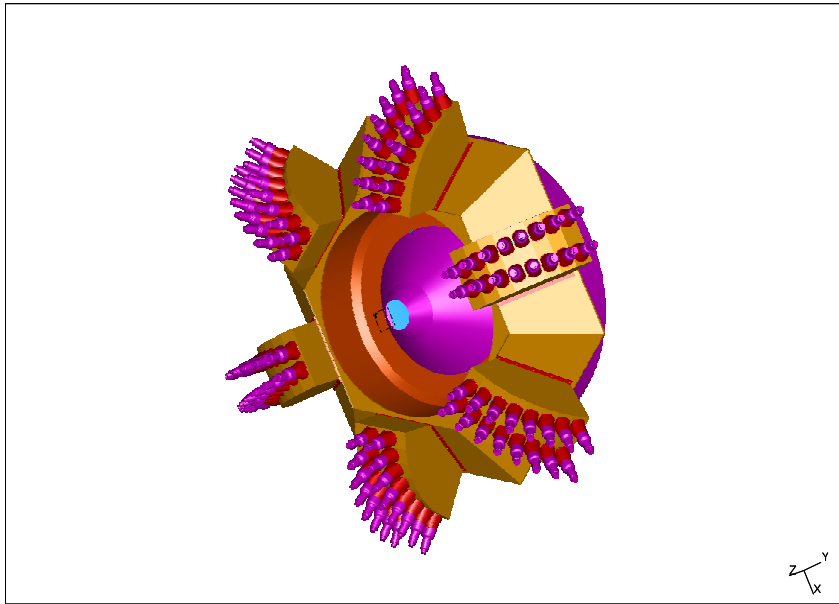


Figure 57: Overall appearance of the appearance of the HTCC, including its mechanical housing

and welded plates of Aluminum.

7.2 PMT Mount

Design analysis of the mirror geometry reveals that the focal points of the mirror combined with their average angles of incidence with their respective PMTs result in a complex surface for mounting the Winston cones, which would involve more expensive material, and a very complex machining sequence. A more simplified surface could be used by repositioning the PMTs along the original light path, up to 2" beyond the planned focal point. This simplification allows the PMT mount surface to be constructed of one plate, bent to each of the angles needed, then welded to sides machined to the same contour as reinforcement. This reduces the cost of manufacturing each mount surface, and would have a negligible effect on beam diameter as it enters the PMT (less than one tenth of an inch increase in beam diameter). Between the axial position and the axial alignment of each Winston cone and PMT on the surface, the position is most critical, and will be set by the machined openings on the surface plate. Alignment of the mirror is the most critical component; there is no need for an alignment structure for each Winston cone/PMT. Figure 58 shows the PMT mounting block design.

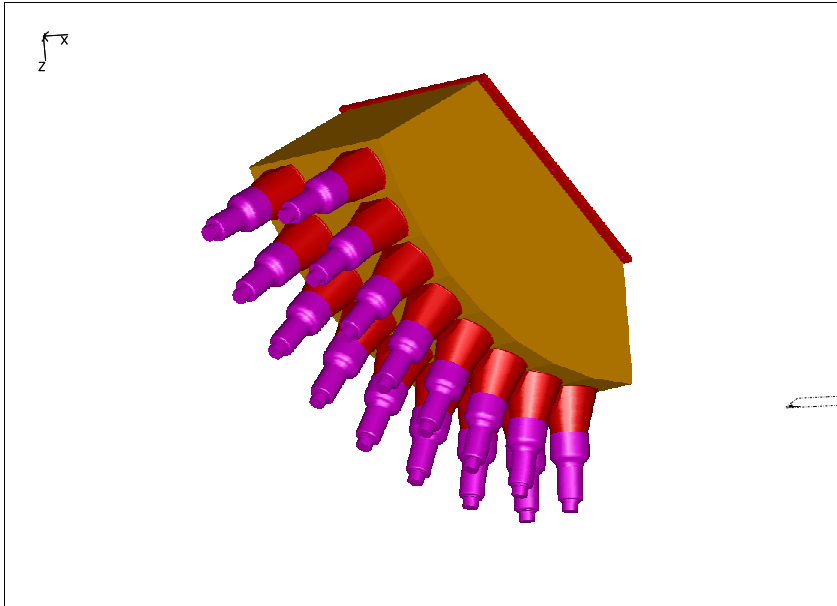


Figure 58: The PMT and Winston cone mounting block.

7.3 Mirror positioning and alignment

Using six dual Boll-Socket adjustment linkages which contact the mirror in three places, the mirror can be securely supported and adjusted in all directions without inducing any force or bending moment except those due to the mirrors own weight. With this system, the mirror would also be protected from possible stresses that the main shell may sustain, whether via temperature changes, transport, maintenance, or other unforeseen forces.

7.4 Upstream and entry

The upstream end of the HTCC must wrap closely around the Central time of flight counters (CTOF) and solenoid, to both avoid interfering with the high θ light paths, and to allow for the greatest possible acceptance angle from the target. This results in a cup-like shape that reaches from the outside of the solenoid, around the forward CTOF lightguides, with a cone in the center that follows the lightguides back in toward the center of the solenoid, stopping just before the SVT. This entry cone must be as thin as possible to retain every available degree of entry angle. Currently, the optimized entry acceptance angle of 33° is limited by the planned solenoid shape, and position of the CTOF lightguides. This angle is only achievable using equipment clearances as low as 5mm, and an entry cone thickness of $.040''$. At this thickness, the cone could be made of aluminum or a carbon composite; it is not a structural member, and only needs to be strong enough to support itself and the entry window. A view

of the presently planned entry structure is shown in Figure 59.

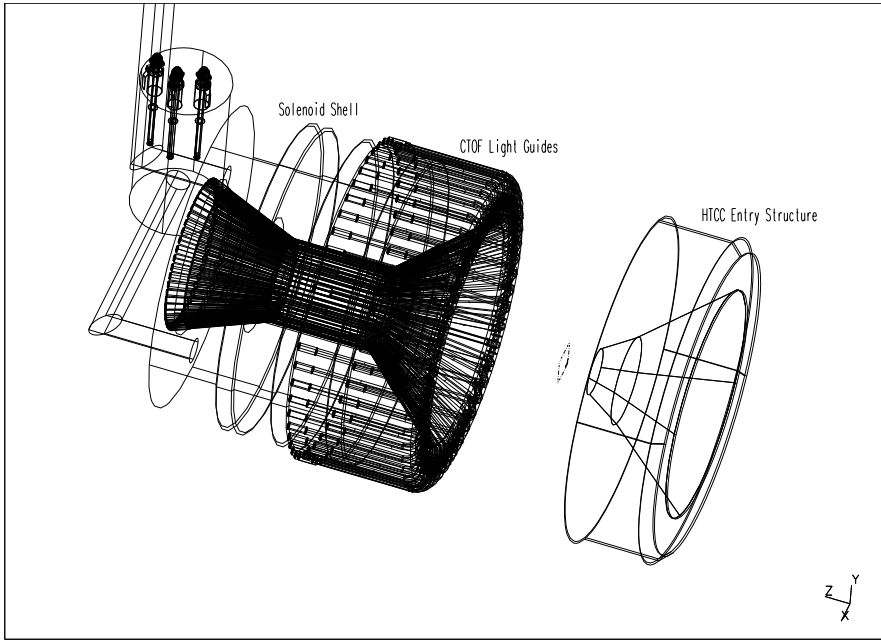


Figure 59: Mechanical entry structure.

7.5 Exit Scheme.

The exit window of the HTTC assembly sets 21mm past the most downstream point of the mirror. As a flat window, it is only possible to achieve 37° acceptance without interfering with region 1 of the torus assembly. To allow charge particles at angles of 40° to pass through the exit window, it must make a bend (near the outer radius of the mirror) and follow the 25° midplane angle of the region 1 assembly. This forms a beveled window, which if made from a carbon/foam composite, would be rigid enough to support itself, and still allow particles to pass through, unobstructed. From the hexagonal portion of the shell where the PMTs are mounted, a cylindrical tube reaches downstream, to house and support the mirror and adjustment fixtures, and finally interfaces with the exit window. The mechanical design of the exit window is shown in Figure 60

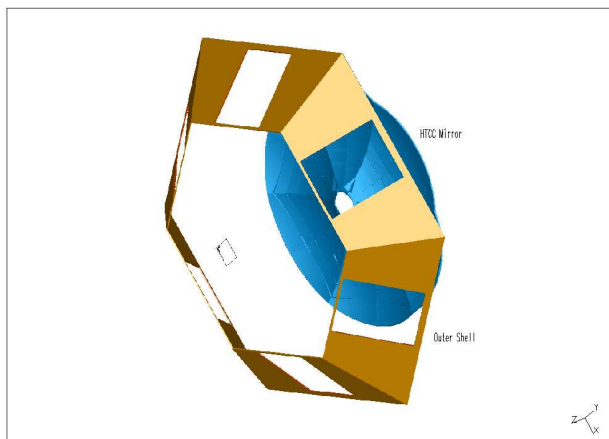


Figure 60: View of the mechanical components of the outer shell.